Title: Microscale physiological events on the human cortical surface detected with PEDOT:PSS Electrodes

Authors: Angelique C. Paulk[1]†, Jimmy C. Yang[1,2]†, Daniel R. Cleary[3,4,5], Daniel J. Soper[1], Sang Heon Lee[6], Mehran Ganji[6], Yun Goo Ro[6], Hongseok Oh[6], Lorraine Hossain[7], Nick Rogers[4], Kivilcim Kiliç[3], Sang Baek Ryu[2], Seung Woo Lee[2], John Hermiz[6], Vikash Gilja[6], Jong Woo Lee[8], Douglas Maus[1], Anna Devor[3], Shelley I. Fried[2,9], Pamela S. Jones[2], Brian V. Nahed[2], Sharona Ben-Haim[5], Ahmed M. T. Raslan[10], Dominic A. Siler[10], Daniel P. Cahill[2], Ziv M. Williams[2], G. Rees Cosgrove[11], Shadi A. Dayeh[5,7,12], Sydney S. Cash[1]

Affiliations:

[1] Department of Neurology, Massachusetts General Hospital, Boston, Massachusetts 02114
[2] Department of Neurosurgery, Massachusetts General Hospital, Boston, Massachusetts 02114.
[3] Departments of Neurosciences and Radiology, University of California San Diego, La Jolla, California, 92093, USA
[4] Department of Physics, University of California San Diego, La Jolla, California 92093, USA
[5] Department of Neurosurgery, University of California San Diego, La Jolla, California, 92093, USA
[6] Department of Electrical and Computer Engineering, University of California San Diego, La Jolla, California 92093, USA
[7] Materials Science and Engineering Program, University of California San Diego, La Jolla, California 92093, USA
[8] Department of Neurology, Brigham and Women's Hospital, Massachusetts 02115.
[9] Boston VA Healthcare System, 150 South Huntington Avenue, Boston, MA 02130
[10] Department of Neurological Surgery, Oregon Health and Science University, Portland, OR, USA
[11] Department of Neurosurgery, Brigham and Women's Hospital, Massachusetts 02115.
[12] Department of Nanoengineering, University of California San Diego, La Jolla, California 92093, USA
†These authors contributed equally to this work: Angelique C. Paulk, Jimmy C. Yang.

*Correspondence: Sydney S. Cash, email: scash@mgh.harvard.edu

Summary

Efforts to deepen our understanding of the nervous system depends on high resolution sampling of neuronal activity. We leveraged clinically necessary intracranial monitoring performed during surgical resections to record from the cortical surface (N=30) using high spatial resolution, low impedance PEDOT:PSS microelectrodes. We identified three classes of activity. The first included relatively fast repeated waveforms with kinetics similar to, but not perfectly matching, extracellular single unit activity. The other two discrete unitary events with slower waveforms had event frequencies which were selectively modulated by auditory stimuli, electrical stimuli, pharmacological manipulation, and cold saline application. Furthermore, different classes had small but significant causal co-occurrences. We speculate that these different events could reflect axonal action potentials, dendritic calcium spikes, backpropagating action potentials or pre and post-synaptic phenomena, opening the possibility that we can sample information beyond typical extracellular somatic action potentials via high-density, low impedance electrodes on the cortical surface.

Keywords

Human cortex, extracellular activity, PEDOT:PSS, electrical stimulation, auditory stimulation

Introduction

Recording and modulating the activity of single neurons, local circuits, and whole-brain network activity are essential to understanding both how the brain supports behavior and in identifying optimal therapies for neurological pathologies. Current research and clinical tools for recording neural activity represent a trade-off between an ability to examine single cell activity as reflected in extracellular recordings of somatic action potentials in relatively small areas

(Chan et al., 2014; Fried et al., 2011; Keller et al., 2010) and record populations of cell firing or populations of synaptic input (as in the local field potential, LFP) over larger areas (Basu et al., 2019; Dykstra et al., 2011). Research in the neurosciences largely focuses on these two ends of the spectrum. Post-synaptic activity, sodium or calcium potentials in the dendritic arbor including back-propagating spikes or localized potentials, have, of course, been a major focus of investigation but are rarely explored in the context of complex behaviors *in vivo* with large-scale circuit analysis, although significant advances in imaging and recording in rodents have begun to come close (Abdelfattah et al., 2019; Suzuki and Larkum, 2017; Yildirim et al., 2019). However, large-scale measures of the full range of circuit dynamics are inaccessible under most experimental circumstances - and certainly not available in recordings from humans. Recent studies, however, have pointed to the possibility that extracellular electrodes can record back-propagating dendritic action potentials (Moore et al., 2017; Robbins et al., 2013; Stuart and Spruston, 2015) or even dendritic calcium spikes both within and from the surface of the cortex (Ross, 2015; Suzuki and Larkum, 2017). Indeed, calcium activity in the form of dendritic action potentials may be detected on the surface of the cortex in rodents (Suzuki and Larkum, 2017). In addition, recent advances in identifying novel neurons in Layer 1 of the human cortex (Boldog et al., 2018) gives one example of neuronal types that might have activity detectable on the cortical surface which may not typically be observed with intraparenchymal penetrating electrodes targeting deeper layers. Finally, the advent of high-density electrodes has also opened the possibility of record travelling axonal action potentials in certain preparations (Bakkum et al., 2013; Barry, 2015). There is an open question as to whether these axonal action potentials could be recorded from the surface of the cortex in humans as well.

PEDOT:PSS electrodes and other novel recording materials have been shown to offer major advantages over traditional electrode designs and fabrication processes which include substantial flexibility in the design, the use of cost-effective materials, and significant reductions in size, both in thickness and area, while increasing channel count (Cellot et al., 2016; Ganji et al., 2017a, 2017b; Khodagholy et al., 2015, 2016; Sessolo et al., 2013; Wilks et al., 2011). These electrodes have also been shown to allow recording of single neuron activity at the pial surface in a variety of preparations (Khodagholy et al., 2017), including in humans (Cellot et al., 2016; Ganji et al., 2017a, 2017b; Khodagholy et al., 2015, 2016; Sessolo et al., 2013; Wilks et al., 2011). We hypothesized that the high density, low impendence capabilities of PEDOT:PSS arrays would allow for the detection of cortical surface activity not readily accessible in recordings from large surface area arrays with large contacts and which may uncover novel activity representative of circuit activity outside of layer 4 and 5 somatic action potentials.

Recordings were made using PEDOT:PSS microelectrodes from patients undergoing craniotomies for the surgical resection of cortical tissue as a result of tumor or epilepsy. The recordings were made alongside clinical neuromonitoring performed as part of the patients' clinical care. We observed both local field potential (LFP) dynamics (typical of pial recordings with metal contacts) (Kaiju et al., 2017) and high frequency events similar to single unit activity as observed in intraparenchymal recordings with penetrating metal contacts (Khodagholy et al., 2015, 2016). In addition, we observed other classes of morphologically and temporally distinct events. All these types of events were also observed in mice (N=4) and a non-human primate (N=1). To determine if these different events were physiological in origin, we investigated their occurrence during auditory and electrical stimulation, during awake procedures and during anesthesia, with pharmacological manipulation, and with the application of cold saline. Finally, we examined how these events were related to each other in time and if they co-occurred.

RESULTS

PEDOT:PSS electrodes record neural activity on the surface of the human brain

We were able to record neural activity from the cortical surface using the PEDOT:PSS microelectrodes in patients undergoing brain surgery for either the removal of tumors (N=14) or for resection in the case of intractable epilepsy (N=16). Electrodes were 30 µm in diameter and had a center-to-center pitch between 50 and 800 µm. Four different electrode designs covering variously-sized areas between 0.1575 and 40 mm^2(see **Methods**; **Fig. 1**) were used. Fabricated on parylene (5-14 um thickness) into either 32 or 128 channel arrays (**Supplemental Fig 2-3**), electrodes were placed directly on and conformed to the pial surface of the exposed cortex. Recordings ranged from 4-25 minutes. With one participant (designated Intraoperative Participant 14, or IP14), the recordings were unstable due to the constant movement of the electrode during the case and were removed from subsequent analyses.

PEDOT:PSS electrodes record fast activity on the surface of the human brain

Following a series of quality control checks of every recording and electrode channel (see **Methods**), we recorded high frequency waveforms as has been demonstrated with other PEDOT:PSS recordings (Khodagholy et al., 2015, 2016, 2017) (**Fig. 1**). We used Kilosort (Pachitariu et al., 2016) to sort waveforms into separable repeated events using a template matching approach (**Fig. 1**). Kilosort identifies clusters of waveforms as repeated events based on the spatial arrangement of the electrode as well as waveform morphology which allowed us to identify putative repeated events with similar waveform shapes across the recording as is done with typical single unit spike sorting (Pachitariu et al., 2016). We found these repeated fast waveform events in most of the recordings (N= 27 out of 29). The sorted waveforms were generally negatively deflecting, with voltage amplitudes 123 ± 101 µV, and with trough to peak widths on average of 0.71 ± 0.32 msec (across 23,055 detected events subdivided into 147 identified, sortable, replicable events detected across 25 recordings; **Fig. 1H**). These average values are within range for what has been recorded using sharp electrodes such as the Utah array in human cortex or even in rodents and non-human primates (Anastassiou et al., 2015; Bartho et al., 2004; Chan et al., 2014; Hamilton et al., 2018; Keller et al., 2010; Robbins et al., 2013; Trainito et al., 2019; Vigneswaran et al., 2011). However, some events had kinetics faster and slower than what may be typical and amplitudes that were sometimes larger than what might be expected at the pial surface for neurons. The implications of this range of event characteristics are discussed below. The average event frequency for each repeated high frequency waveform across participants was 0.29 ± 1.16 Hz (**Fig. 1I**). Inter-event interval histograms showed a wide variety of intervals across participants (**Fig. 1J**).

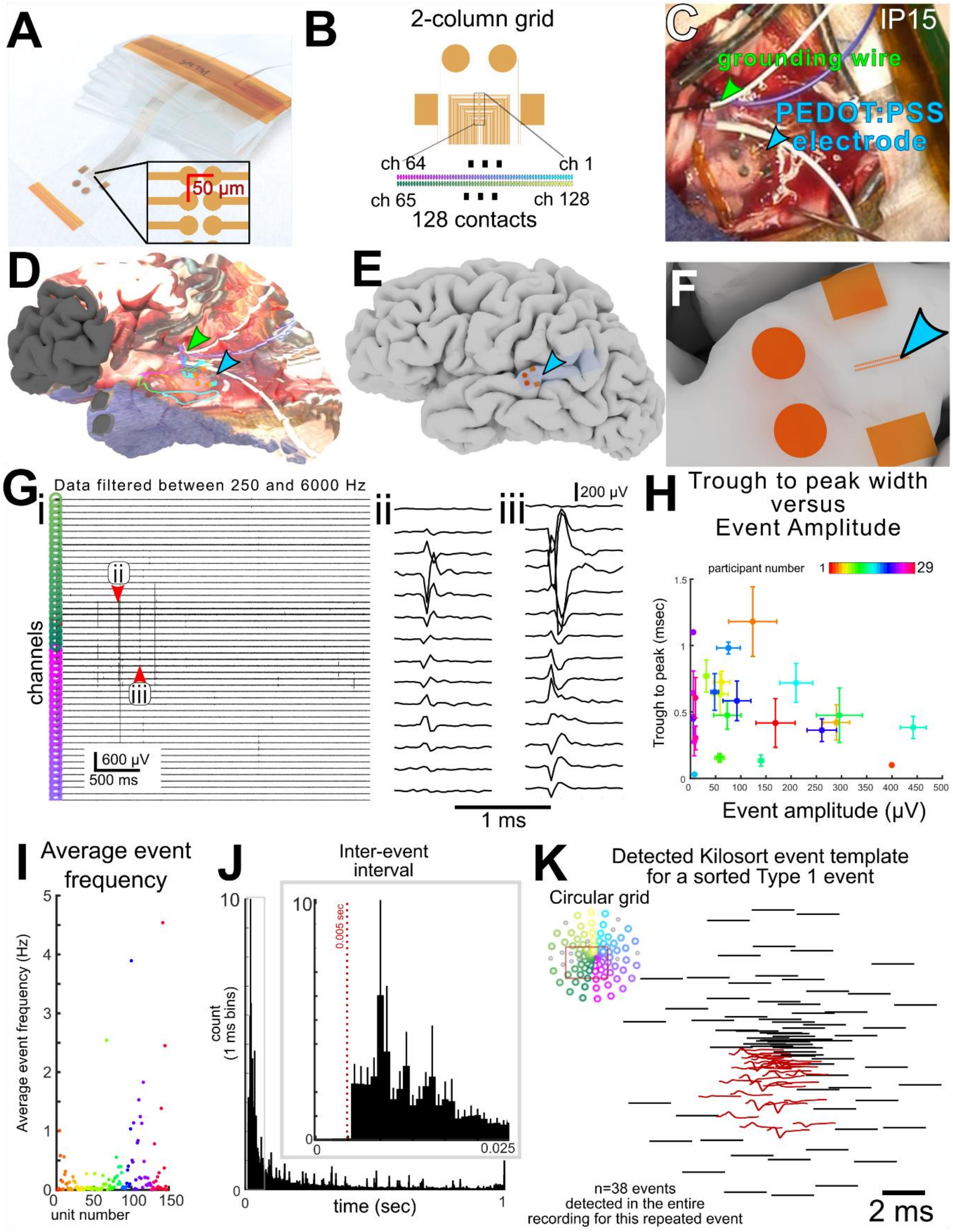

Figure 1. PEDOT:PSS recording set up and high frequency waveform events on the surface of the human cortex. **A-B**. PEDOT:PSS 2-column grid electrode layout and dimensions,

including (**A**) the size of the electrode and (**B**) the orientation of the 128 channels. **C**. Image of the PEDOT:PSS (blue arrowhead) on the surface of the human cortex alongside reference electrodes (green arrowhead) and a clinical strip electrode. **D**. Image from (**C**) projected on a 3D reconstruction of the participant's brain (IP15). **E**. Location of the PEDOT electrode on the 3D reconstruction the brain, along with (**F**) a zoomed-in version of the electrode. **G**. Example recording from participant IP11. The color coding of cyan to magenta (channels 1-64) then from green to yellow (channels 65-128) correspond to the channels on the 2-column map as indicated to the left. In **i**, **ii** and **iii** designate the traces which are then shown to the right at a higher resolution. **H**. Trough to peak and peak to peak amplitudes of the sorted waveforms were compared across participants. error bars indicate s.e.m., N=29. **I**. Average event frequency in Hz with error bars indicating s.e.m. Participant number is color coded as in the color bar indicating participant number shown in **H**. **J.** Average Inter-event intervals across participants, N=29, and **K.** Template for a fast Type 1 event detected using Kilosort showing the waveform distribution across the array.

PEDOT:PSS electrodes detect slower, local, discrete, classifiable events on the surface of the human brain

Spatially and temporally localized events, which were distinct from the fast waveform activity, was also detectable with these electrodes (**Fig. 2A, B**). These events occurred across multiple channels in a single recording and varied in polarity across channels and in time (**Fig. 2A, B**). Notably, these events demonstrated separable time courses, with some events on the time scale of 100-200 ms in duration and others less than 20 ms with separable waveforms occurring even on the same channel in a given recording (**Fig. 2A-D**). These events could repeat through time across neighboring channels (blue circles: repeated event 1; orange circles: repeated event 2; **Fig. 2D**). Events were not restricted to a single amplifier bank, cable, or other physical structure (see **Methods; Fig. 2A-D**). Since these events were repeatedly observed across cases and recordings, we set out with the goal of classifying, and characterizing, these waveforms as discrete events to determine if these events are neurophysiological in origin and if they can be modulated, and if these events have a significant relationship to the detected fast waveforms (**Fig. 1**).

Since the duration of many of these identified events was longer in time than that of single unit waveforms and, in some cases, resembled calcium spikes in their duration[3,18,20], we classified all events as either 1) Type 1: fast repeated waveform events, detected between 250 and 6000 Hz (**Fig. 1**); 2) Type 2: peaks with a sharp rise and slow fall, ~10-30 ms absolute half-peak duration, detected below 500 Hz; or 3) Type 3: peaks with a slow rise and slow fall, ~100 ms absolute half-peak duration, detected below 500 Hz (**Fig. 2A-F**). This division was based on both frequency bands in the voltage signals and principal components analysis combined with k-means clustering approaches. First, Type 1 events were found in the frequency range between 250 and 6000 Hz while Type 2 or 3 events were identified in low pass filtered voltage below 500 Hz. Due to the high frequency components of the Type 1 events, we could then use commonly used spike sorting strategies to detect and identify repeated Type 1 events (**Fig. 1**). Lower frequency events below 500 Hz, however, were more variable in duration and size or could overlap considerably more than the fast Type 1 events (**Fig. 2**), making typical spike sorting approaches difficult even if we widened the detection window for the lower frequency band.

Therefore, we used PCA combined with k-means clustering to identify the most common baseline waveforms for putative Type 2 and 3 events (**Supplemental Figure 7**). From this PCA and clustering approach, we derived waveform templates which were then used in template matching to identify individual Type 2 and Type 3 events, their timing and channel location throughout the recordings. Waveforms received an event tag of Type 2 or 3 if their correlation with a single template event waveform exceeded 0.8 (**Fig. 2E, F**; see **Methods**). This was followed by an additional filtering step that thresholded events based on their maximum second derivative (see **Methods**).

Type 2 events had an average RC time constant rise time ($\tau_{\text{rise time}}$) of 14.18 ± 8.42 ms and RC time constant decay time ($\tau_{\text{fall time}}$) 30.62 ± 6.33 ms as averaged across participants (after taking the absolute voltage values). In contrast, Type 3 events had $\tau_{\text{rise time}}$ of 28.62 ± 8.80 ms and $\tau_{\text{fall time}}$ of 81.48 ± 11.91 ms. As a confirmation that the template matching approach can be used to detect separable Type 2 and 3 events, the differences in $\tau_{\text{rise time}}$ and $\tau_{\text{fall time}}$ were significantly different between event types (following averaging values per patient and then comparing between types; N=30; $p<0.00001$; Wilcoxon rank-sum test; **Fig. 2G-Gii**). In addition, Type 3 events were significantly more frequent than Type 2 events ($p<0.0001$; Wilcoxon rank-sum test; **Fig. 2Giii**), with Type 3 events (n=145,219) occurring ~16 times more often than Type 2 events (n=9,522) across recordings across participants. To confirm that these events were repeatable in time and space, we calculated the variance of the detected Type 2 and 3 events across channels and within channels. We found the variance in the voltage across channels was larger than within channels (**Supplemental Figure 7**). While this difference was not significant ($p>0.05$, Wilcoxon rank sum test, **Supplemental Figure 7**), the strict use of a template matching approach likely limited how different the waveforms could be between and across channels.

We did not observe significant differences between the epilepsy versus tumor surgical intervention cases (**Supplemental Tables 1-2**) for all Type 2 and 3 waveform metrics in these recordings ($p>0.05$; Wilcoxon rank-sum test; **Fig. 2Gi-Giv**). Interestingly, the only significant difference we could find between surgical cases was that the Type 3 rise times were significantly longer in awake cases (0.16 ± 0.106 sec) than in the anesthetized (0.08 ± 0.071 sec) cases ($p=0.0170$, Wilcoxon rank-sum test; ranksum=136). In multiple patients, we were able to confirm the presence of Type 2 and Type 3 events in multiple brain regions by both sampling across brain regions between cases and, in eight instances, moving the electrode to different brain areas during the recording (**Supplemental Fig. 1-3**). There were no significant differences between recordings in the temporal lobe and other areas of the brain which included the dorsolateral prefrontal cortex, motor area (precentral gyrus), and the parietal lobe ($p>0.3250$; Wilcoxon rank-sum test).

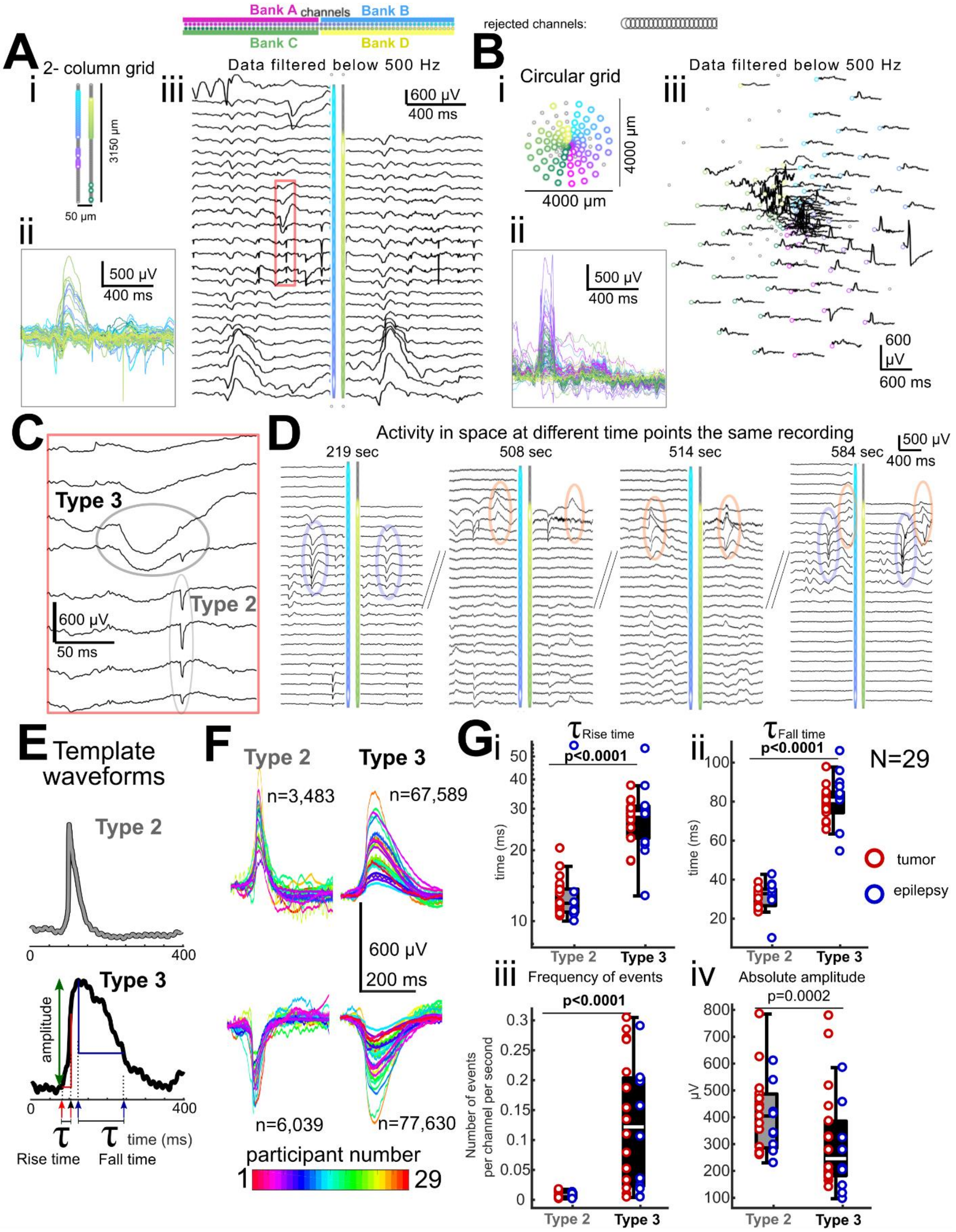
Bank A
channels
Bank B
Bank C
Bank D
rejected channels:
A
i
2- column grid
3150 μm
50 μm
ii
500 μV
400 ms
iii
Data filtered below 500 Hz
600 μV
400 ms
B
i
Circular grid
4000 μm
4000 μm
ii
500 μV
400 ms
iii
Data filtered below 500 Hz
600 μV
600 ms
C
Type 3
Type 2
600 μV
50 ms
D
Activity in space at different time points the same recording
219 sec
508 sec
514 sec
584 sec
500 μV
400 ms
E
Template waveforms
Type 2
0
400
Type 3
amplitude
0
400
τ
τ
time (ms)
Rise time
Fall time
F
Type 2
Type 3
n=3,483
n=67,589
600 μV
200 ms
n=6,039
n=77,630
participant number
1
29
G
i
τ Rise time
p<0.0001
time (ms)
10
20
30
40
50
Type 2
Type 3
ii
τ Fall time
p<0.0001
time (ms)
20
40
60
80
100
Type 2
Type 3
N=29
tumor
epilepsy
iii
Frequency of events
p<0.0001
Number of events per channel per second
0
0.05
0.1
0.15
0.2
0.25
0.3
Type 2
Type 3
iv
Absolute amplitude
p=0.0002
μV
100
200
300
400
500
600
700
800
Type 2
Type 3

Figure 2. Classifiable events can be identified across recordings and participants. **A**. Example recording (electrodes which passed criteria, **Ai**) from participant IP15 showing activity changes in time (**Aii**) and a proportion of electrodes and their activity mapped to the two-column electrode array (**Aiii**). **b**. Recording from participant IP25 in time (**Bi-ii**) and mapped to the circular grid (**Biii**). The color coding of the waveforms match the color coding of the channels with magenta, yellow, green, and cyan color coding indicating the four separate 32 channel amplifier banks used in the recording. **C**. Zoomed view of the red box in **Aiii** showing Type 2 and 3 events. **D**. Example recordings of events at different time points (for IP15) showing only a subset of electrode channels. Repeated events through time for two different event examples are shown (orange and blue ovals). **E**. Template waveforms used to classify the activity. Measurements include baseline activity before the onset to the peak amplitude (green arrow), the rise and fall times relative to the peaks (see methods) by quantifying the $\tau_{\text{rise time}}$ and $\tau_{\text{fall time}}$ time constants as in the following equation: $\Delta V = (V_{\text{final}} - V_{\text{start}})*(1\text{-}1/e\text{\^{}}(\text{time}/\ \tau))$, where $\tau_{\text{rise time}}$ was calculated as time it took for the voltage to reach 0.63 of the maximum peak (red arrows) and $\tau_{\text{fall time}}$ was calculated as the time it took for the voltage to reach 0.37 of the fall back to baseline (blue arrows). **F**. Average waveforms per participant (N=29) for the different classes of events. **G**. Average $\tau_{\text{rise time}}$ (**Gi**), $\tau_{\text{fall time}}$ (**Gii**), frequency of events (**Giii**), and absolute amplitude (**Giv**) per waveform type across participants, shown in box plots with confidence bounds. N=29. p-values are for comparisons between waveform types, Wilcoxon rank-sum comparison. Center lines indicate median, box limits indicate confidence bounds. All voltage data shown was derived from raw data which was filtered below 500 Hz.

Event Types have Different Spatial Characteristics

The spatial spread of these Type 2 and 3 events could aid in identifying, and possibly differentiating, their neural substrates (Bakkum et al., 2013; Barry, 2015; Suzuki and Larkum, 2017). Defining spatial spread as the number of channels showing an event within a 10 ms time window (chosen based on the distribution of inter-event intervals; **Fig. 3A-B**), we found the number of non-overlapping windows with single Type 2 or Type 3 events was larger than, though not significantly different from, the number of windows with multiple Type 2 or Type 3 events across multiple channels (**Fig. 3B**). The proportion of windows with multiple Type 2 events (17.92 ± 2.59%) was less than that of windows with Type 3 events (30.08 ± 3.16%), though this difference was not significant. On average, 70.12 % (± 3.09%) of all detected Type 2 and 3 events were isolated on single channels (**Fig. 1**). Thus, Type 2 and 3 events can be isolated on single channels or observed across multiple channels with a trend of Type 3 spreading further than Type 2 events.

We then examined windows with multiple events and, for each window, measured the average number of detected waveforms (events), distance in space from the start to end of the multi-event window (in µm), the area covered (in µm^2), the speed of the events (in m/sec), and the time range covered by all the events within each type (sec). The number of detected waveforms per window, the spatial distance, and the spatial area were not significantly different between Type 2 and Type 3, though multichannel Type 3 events tended to cover more area and spatial distances ($p>0.0704$; Wilcoxon rank-sum test; **Fig. 3C**). Notably, both Type 2 and Type 3 events were, on average, observed across 5-10 channels across the entire array across participants, further supporting the idea that they are relatively localized (**Fig. 3C**).

However, the Type 3 events were significantly faster ($p=0.0401$; ranksum=114; Wilcoxon rank-sum test) and, similarly, spanned a larger range of time per detected window (p=0.0216; ranksum=108; Wilcoxon rank-sum test; **Fig. 3Civ-Cv**) though a confound was that there were some differences in the spatial spread between the larger circular grid compared to the smaller 2-column grid (as indicated by the deep purple versus orange scatter plots; **Fig. 3Cii**, **Ciii**). We found that the average speed of the events across the array was around half the speed of slow unmyelinated axonal action potentials (Bakkum et al., 2013; Barry, 2015), though there was considerable variability in the speeds of events per participant (Speed Type 2: 0.04 ± 0.01 m/sec; Speed Type 3: 0.05 ± 0.03 m/sec; **Fig. 3Civ**).

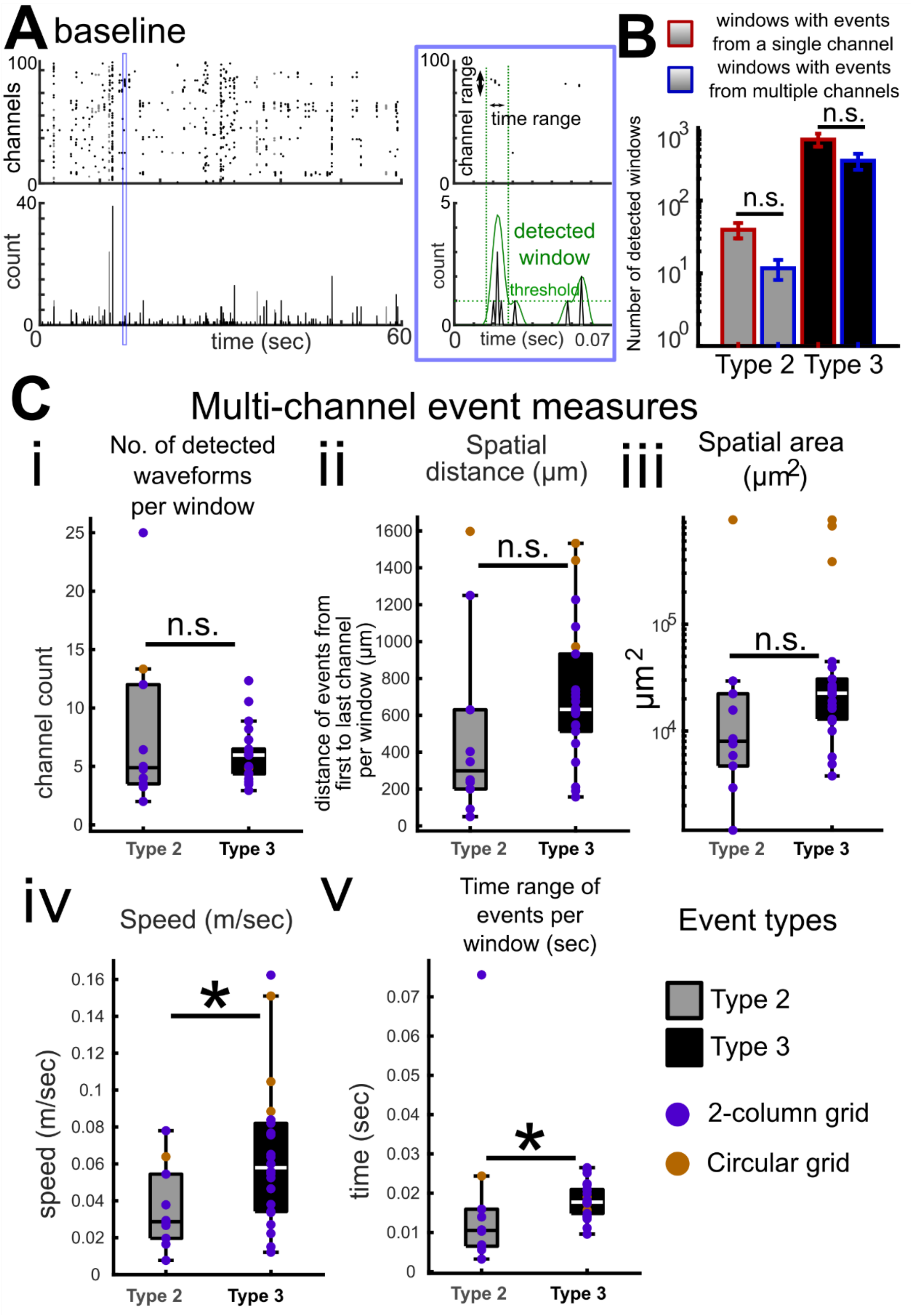
A baseline
100
channels
0
40
count
0
0
time (sec)
60
100
channel range
time range
0
5
count
detected window
threshold
0
0
time (sec)
0.07
B
windows with events from a single channel
windows with events from multiple channels
n.s.
n.s.
Number of detected windows
10^3
10^2
10^1
10^0
Type 2 Type 3
C
Multi-channel event measures
i
No. of detected waveforms per window
channel count
25
20
15
10
5
0
n.s.
Type 2
Type 3
ii
Spatial distance (μm)
distance of events from first to last channel per window (μm)
1600
1400
1200
1000
800
600
400
200
0
n.s.
Type 2
Type 3
iii
Spatial area (μm^2)
μm^2
10^5
10^4
n.s.
Type 2
Type 3
iv
Speed (m/sec)
speed (m/sec)
0.16
0.14
0.12
0.1
0.08
0.06
0.04
0.02
0
*
Type 2
Type 3
V
Time range of events per window (sec)
time (sec)
0.07
0.06
0.05
0.04
0.03
0.02
0.01
0
*
Type 2
Type 3
Event types
Type 2
Type 3
2-column grid
Circular grid

Figure 3. Temporal and spatial spread of Type 2-3 events. **A**. Recording from participant IP17 overlapping time windows when events detected across channels occur close to each other in time during baseline activity, with an illustration of detecting the windows with multiple events 10 ms relative to each other (blue box). **B**. Number of windows with single Type 2 and Type 3 events (isolated events) versus windows with multiple Type 2 and Type 3 events across participants. n.s.; not significant, $p>0.05$, Wilcoxon rank sum test. N=29. Error bars are s.e.m. **Ci-v**. Of the windows with multiple detected events per window, we compared the detected waveforms (events) per window, time range covered by all the events within each type per detected window (sec), the area covered (in μm^2), the speed of the events (in m/sec), and the distance in space from the start and end of the multi-event window (in μm) between Type 2 and Type 3 events. Plots include box plots and confidence bounds of the mean values per measure per participant indicated by whisker plots, center line indicates median, N=29. Asterisks indicate $p<0.05$, Wilcoxon rank sum test.

Spectral Dynamics Surrounding Type 1, 2 and 3 Events

Known single unit activity as well as LFP evoked potentials have been shown to lock to different frequencies or LFP voltage deflections (Khodagholy et al., 2015, 2016, 2017) and have been shown to be involved in behavioral and cognitive processing (Ossmy et al., 2015). We calculated the event-triggered normalized power dynamics for the Type 1, Type 2, and Type 3 events for five different frequency bands (2-4 Hz, 4-8 Hz, 8-15 Hz, 15-30 Hz, 30-55 Hz, 65-200 Hz; normalized to all windows for the ±10 seconds around each event; **Supplemental Fig. 11**). Type 1 events corresponded with an average broad band peak only over the duration of the event, when the event differed significantly from baseline (.25 ms before the event) for multiple frequency bands (4-30 Hz) (**Supplemental Fig. 11**). Type 2 events coincided with a significant broadband increase in power slightly before and during the event followed by a significant decrease in power afterward in the high gamma range (65-200 Hz) power ($p<0.001$; Wilcoxon rank sum test; corrected for multiple comparisons with false discovery rate control; **Supplemental Fig. 11**). Type 3 event-triggered LFP power had peaks in low frequency power around each event which were smaller than around the Type 2 events (**Supplemental Fig. 11**). We performed the same event-triggered power calculation on the few detected 'events' in saline recordings (see **Methods**) and found no such increase in power at the onset of the event and no suppression in high frequency activity after the event (**Supplemental Fig. 12**).

Type 1-3 events are detectable in other species

To examine the contention that these events do not represent normal neuronal activity as they could be small-field inter-ictal discharges (IIDs) in epileptiform tissue (Curtis et al., 2012), and in preparation for future, more extensive mechanistic investigations (Abdelfattah et al., 2019; Barry, 2015; Moore et al., 2017; Suzuki and Larkum, 2017), we examined the presence of these events in animal preparations which would not have the possible confounds of coming from brain tissue adversely characterized by tumor or epilepsy. These investigations included recordings from the barrel cortex region of the primary somatosensory cortex (S1) of an anesthetized mouse (N=1), primary visual cortex (V1) in a ketamine-anesthetized mouse which was subsequently euthanized, primary visual cortex (V1) in two isoflurane-anesthetized mice, and both primary and higher visual areas (VI and V4) in an anesthetized non-human primate (NHP) in an acute setting (N=1) using the circular, 2-column, and square grid electrodes (**Supplemental Fig. 5, 6, 13**). In the subdural recordings (in the NHP and mouse barrel cortex), we found Type 1, 2, and 3 waveforms across recordings and repeatedly in the same recordings, while we found only Type 2 and 3 waveforms in the V1 mouse epidural recordings, possibly due to the low-pass filtering property of the dura (**Supplemental Fig. 13;** Type 1 activity data not shown). The Type 2 and 3 all had waveform characteristics ($\tau_{\text{rise time}}$ and $\tau_{\text{fall time}}$) and frequencies similar to what was seen in the human recordings (**Supplemental Fig. 13-14**). We also performed the event-triggered spectral comparison and found dynamics similar to that in humans (**Supplemental Fig. 15**). Finally, we performed a test of euthanizing a mouse and recording over the same V1 area of cortex as was recorded in the ketamine-anesthetized preparation over the same cortex. We found the Type 1, Type 2, and 3 waveforms completely disappeared (**Supplemental Fig. 13**).

Physiologically-relevant Manipulations Alter Event Dynamics in Human Recordings:

Auditory Stimulation Increases Type 3 Events

An essential question concerning these events is whether they represent neuronal activity relevant to behavior such as sensory processing. We were able to record neural activity over the superior temporal gyrus (STG) while presenting regular auditory cues in a subset of participants undergoing awake resective surgeries (Ganji et al., 2017; Hermiz et al., 2018) (N=8; **Fig. 4A-B**). Across participants, we detected both evoked potentials and Type 1-3 events that were related to the auditory task (**Fig. 4C**; see **Methods**). We calculated peristimulus time histograms (PSTHs) for the Type 1-3 event frequencies around each auditory cue and, when we subdivided the trials into the noise-vocoded sounds, real syllables, and nonsense syllables (**Fig. 4E**; see **Methods**), we found the Type 1 events increased in frequency following the real word syllable sounds, though the difference was not significant either in the change in frequency or the z-scored counts (**Fig. 4D-E**). We found no significant difference in counts for Type 2 events (**Fig. 4F-G**), but there was a significant increase in the Type 3 event counts relative to baseline for the real word syllable and nonsense syllable trials (**Fig. 4H-I**, event frequency (Hz) comparison: p=0.0022; Wilcoxon rank sum test). Interestingly, Type 3 z-scored counts were significantly different between trial types (p<0.00001; z-scored relative to the 0.25 sec before the auditory cue; Kruskal-Wallis multiple comparisons test; **Fig. 4I**). We did not find significant differences in the characteristics of waveforms occurring during the auditory cue versus outside the cue epochs (**Supplemental Fig. 16).**

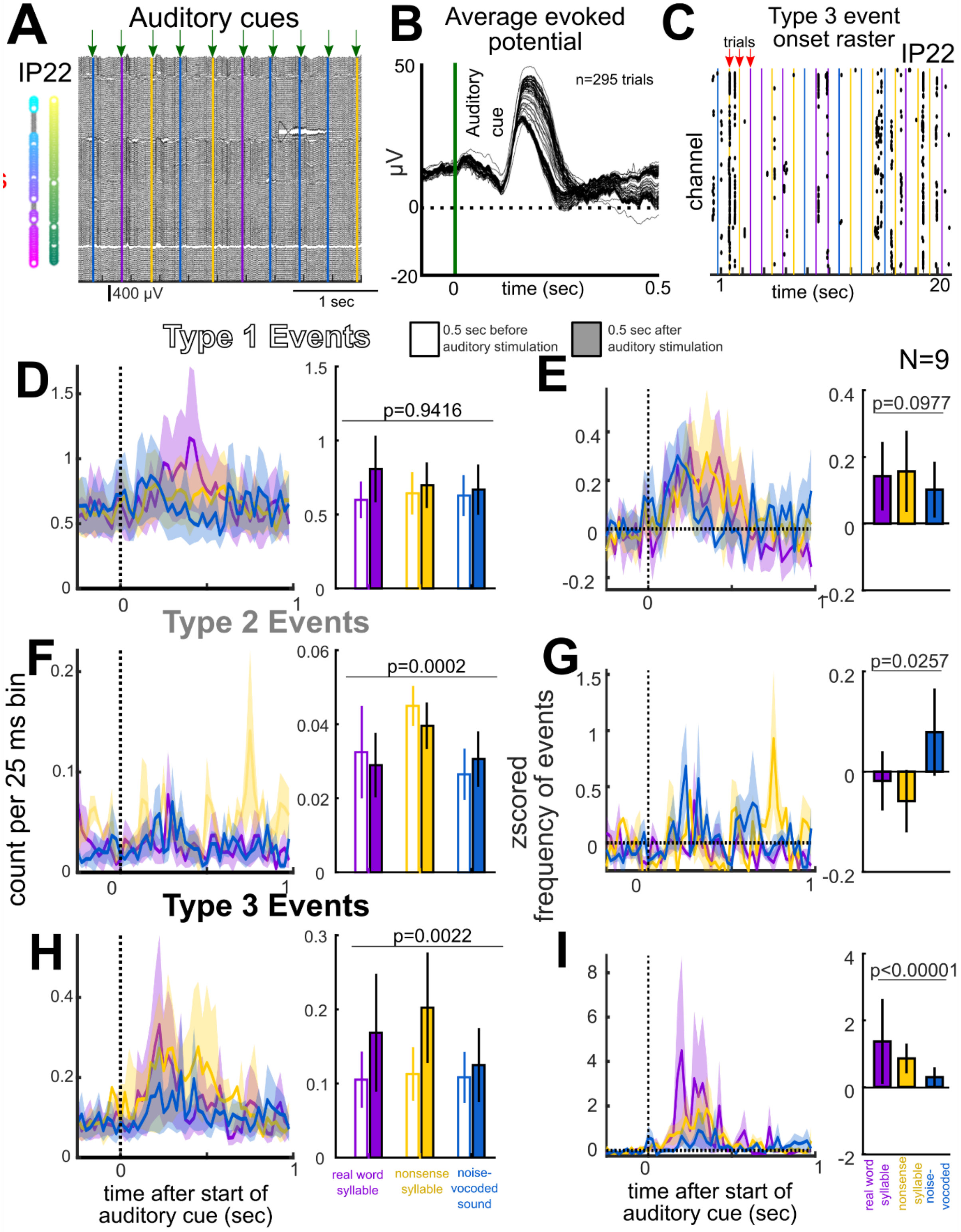

Figure 4. Effects of auditory stimulation on Type 2-3 events. A. Recording from participant IP22 showing neural dynamics during the presentation of repeated auditory stimuli. **B**. averaged

evoked potentials across trials. **C**. Raster plots of Type 3 events occurring across all trials with the timing of the trials indicated by vertical lines, purple lines: real syllable trials; yellow lines: nonsense syllable trials; blue lines: noise-vocoded trials. **D,F,H**. Left: Peri-stimulus time histograms (PSTHs) of each event type binned per 25 ms . Right: bar graphs are mean counts at baseline and from the 0.5 sec after auditory stimulation. **E,G,I**. Left: z-scored normalized peri-stimulus time histograms (PSTHs) of each event type binned per 25 ms around auditory stimulation trials (z-scoring performed relative to 0.25 sec before auditory stimulation). Right**:** Mean z-scored counts relative to baseline from the .5 sec after auditory stimulation. p-value indicates significant difference across conditions, Kruskal-Wallis multiple comparisons test, N=9. Color coding throughout as in **c**. For the line plots, shaded error regions are all s.e.m. For the bar plots, error bars are all s.e.m.

Pharmacological Manipulation Alters Event Frequency

Further testing on whether these Type 1, 2, and 3 events are neurophysiological included the application of cold saline (N=7) or the administration of pro-convulsant agents intravenously (methohexital or alfentanil) to map seizure foci in the brain (Curtis et al., 2012) (N= 8; **Supplemental Table 1-2**). Across participants, both the addition of cold saline and pro-convulsant medication such as methohexital suppressed the frequency of events, particularly the Type 1 and Type 3 events (**Fig. 5A-B**). Specifically, administration of pro-convulsant medication resulted in a significant decrease in frequency three minutes after the medication was intravenously injected for the Type 1 events (7.76 ±15.87 Hz before injection vs 0.01 ± 0.02 Hz three minutes after injection). A decrease in frequency was also observed for the Type 3 events (4.84 ± 4.57 Hz before injection vs 0.12 ± 0.17 Hz three minutes after injection), with both decreases continuing up to 5 minutes (N=8; **Fig. 5A-B, left column**). There was a trend for Type 2 events to decrease from before (0.12± 0.09 Hz) to three minutes after (0.0083 ± 0.0081 Hz) the addition of pro-convulsant medication though it was not significant which could have to do with the low overall rate. We contrasted these results with changes in the frequency of identified interictal discharges (IIDs) which are indicative of epileptiform activity and are defined as events of ~250 ms duration (Curtis et al., 2012) as identified by trained epileptologists. We found the frequency of IIDs following the application of pro-convulsant medication increased significantly (0.0010 ± 0.0011 Hz before injection vs 0.0099 ± 0.0094 Hz three minutes after injection; N=8; **Fig. 5A-B, left column**).

The addition of cold saline suppressed Type 1-3 events across participants (N=7; **Fig. 5A-B, right column**). Type 1 event counts decreased from 0.69± 0.63 Hz to 0.02 ± 0.04 Hz one minute after cold saline application. Type 2 event frequency decreased from 0.71 ± 0.96 Hz during baseline to 0.01 ± 0.02 Hz two minutes after the application of cold saline across all channels across participants with the cold saline taking 1-2 minutes to take effect. The frequency of Type 3 events also changed with cold saline, with a significant decrease after 2 minutes (3.05 ± 2.44 Hz before addition of cold saline vs 0.09 ± 0.11 Hz two minutes after saline addition; $p<0.0001$; Kruskal-Wallis multiple comparisons test; **Fig. 5A-B,** right column).

While these manipulations altered event frequency, the addition of cold saline and pro-convulsant medication did not significantly alter waveform characteristics relative to baseline ($p>0.12$; Wilcoxon rank sum test; **Supplemental Fig. 16**). In all cases, room temperature saline was regularly used to prevent drying out of the brain during the course of all the recordings, but, in contrast to the cold saline, we found no noticeable change in the event frequency during the application of this room temperature saline (data not shown).

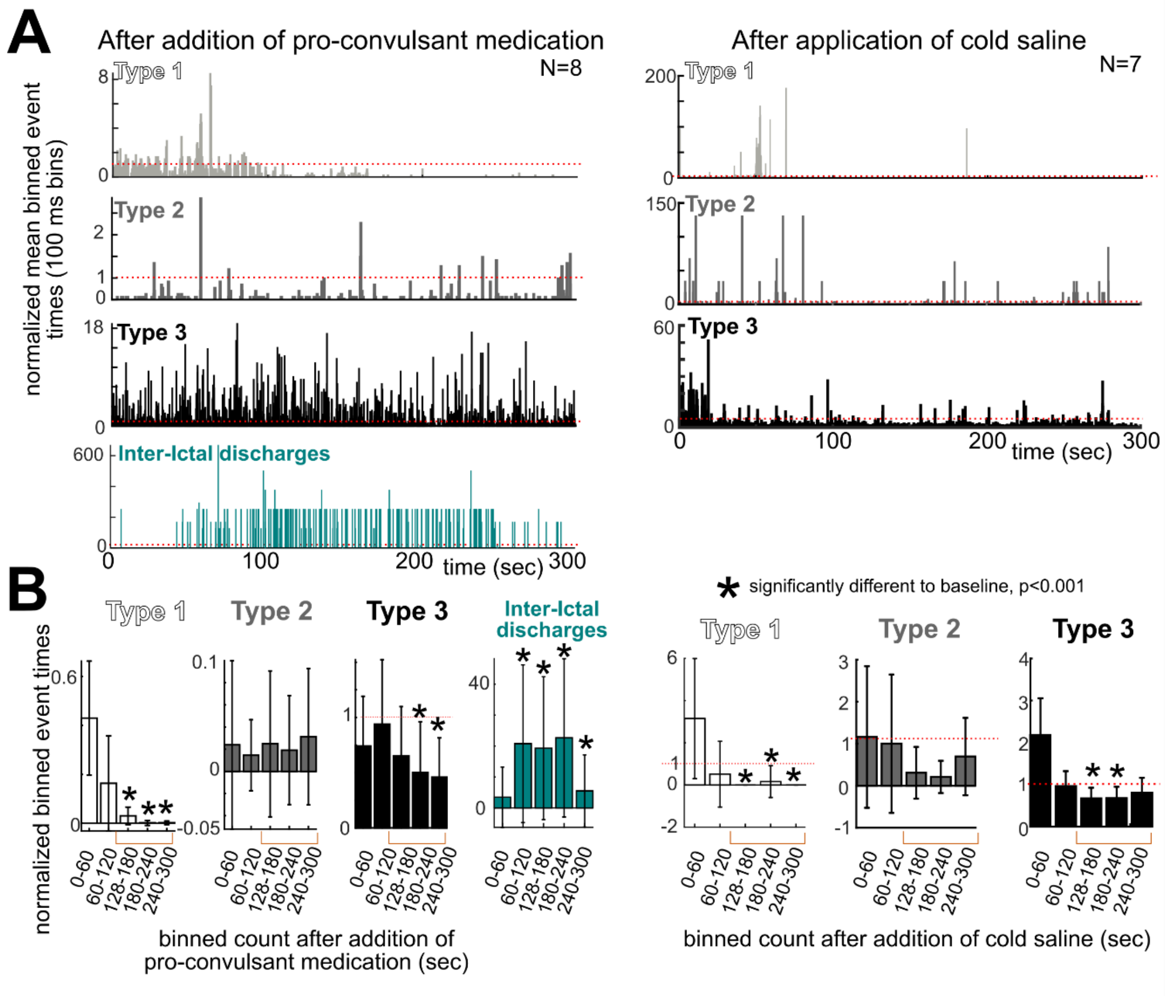

Figure 5. Physiological effects on detected Type 1, Type 2, Type 3 events and inter-ictal discharges. **A**. Peri-stimulus time histograms of binned activity following the application of pro-convulsant medication (methohexital or alfentanil; left) or the application of cold saline (right) averaged across patients. Type 1 (top), Type 2 (middle), Type 3 events (middle) and inter-ictal discharges (IIDs, bottom) were binned every 100 ms and normalized relative to baseline by dividing each bin by the average baseline activity. Dotted red line is the baseline normalization value. **B**. Histogram of activity changes with 5-minute bins, error bars are SEM, N=8 for pro-convulsant medication, N=7 for cold saline application. Asterisks indicate significant difference from baseline with p<0.001, Wilcoxon rank sum test. Error bars are all s.e.m. in **B**.

Electrical Stimulation Changes the Frequency and Spread of Events

Further testing the hypothesis that Type 1-3 events are neural in origin, we examined changes in activity during and after trains of electrical stimulation (as in motor or language mapping (Berger and Ojemann, 1992; Borchers et al., 2012; Kawaguchi et al., 1996; Mueller and Morris, 1993; Viventi et al., 2011), **Fig. 6A**). Remarkably, when trains of stimulation were applied to the surface of the cortex, we observed induced travelling waves of Type 3 events progressing across all channels, sometimes starting soon after the end of stimulation but often arriving 1 to 2 seconds after local stimulation (**Fig. 6A**; activity in time). This propagating wave of activity was observed in all instances where clinically relevant trains of electrical stimulation were used in the surgical case (N=8). Such delayed waves of activity have been reported in other situations as well in other cortical recordings (Viventi et al., 2011), though not due to stimulation.

We examined the PSTH around each stimulation train (normalized to the 1 second before stimulation) and found that, during stimulation, there was a significant increase of Type 1 events while, at the same time, there was significant inhibition of the Type 2 and 3 events ($p<0.0001$; Wilcoxon rank sum comparison between baseline and each binned time window; **Fig. 6B-C**). Immediately after stimulation, in contrast, both Type 2 and 3 events significantly increased in frequency (**Fig. 6B-C**). Interestingly, Type 1 events decreased significantly after stimulation ($p<0.001$; Wilcoxon rank sum comparison between baseline and each binned time window**; Fig. 6B-C**). Once again, waveform characteristics did not change significantly (**Supplemental Fig. 16**).

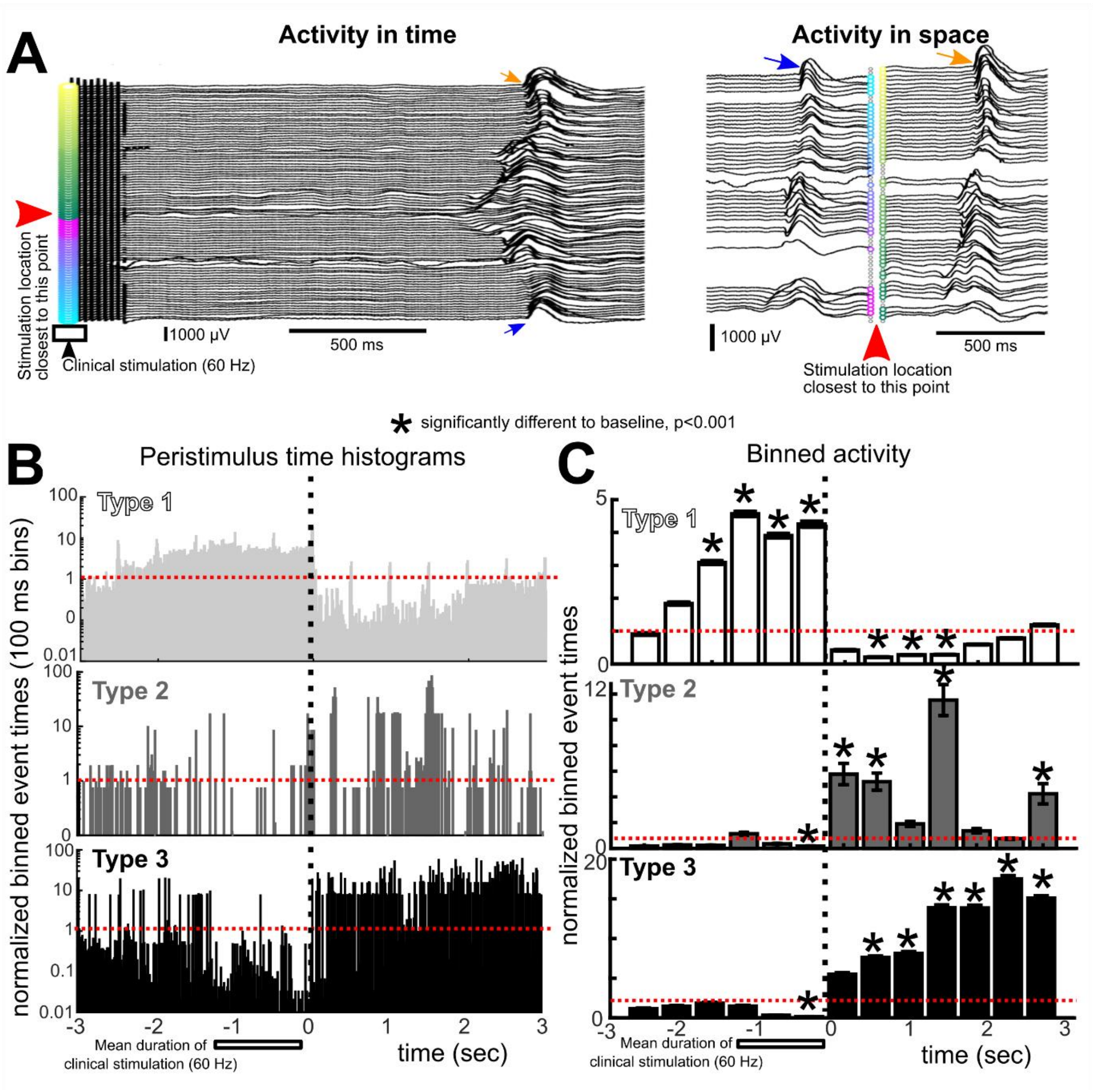

Figure 6. Electrical stimulation induces changes in the frequency of Type 1-3 events. **A**. Recording from participant IP07 showing a wave of activity (Type 3 event) following a train of 60 Hz stimulation during clinical mapping, shown in time (left) and mapped relative to the electrode layout (activity in space, right). Blue and orange arrowheads indicate the same channel pairs in the time and space comparison. The red arrowhead indicates the relative direction and location of stimulation. The blue and orange arrows correspond to the same channels in the left and right groups of traces, with the Type 3 events laid out per the physical architecture of the 2-

column electrode in the right traces. **B**. Peri-stimulus time histograms of binned activity around the time of stimulation (bar below figure) averaged across patients (N=8, n>5 trials per participant). Type 1 (top), Type 2 (middle), and Type 3 (bottom) events were binned every 100 ms and normalized relative to the 1 sec before stimulation. The dotted red line is the normalized baseline value. Note: the y-axis is in log scaled increments. **C**. Histograms of activity in 0.5 sec bins before and after stimulation. p-values are a result of testing differences between each 0.5 sec bin per event type, N=8. Asterisks indicate significant difference from baseline with p<0.001, Wilcoxon rank sum test. In **c**, error bars are all s.e.m.

Temporal and Spatial Interactions between Different Event Types

What are the temporal relationships amongst these different events? We examined whether the Type 1 events had a consistent relationship to the slower Type 2 and 3 events (**Fig. 7**). We found there were several examples across participants where there were concurrent Type 1, 2, and 3 events seemingly overlapping in time or with Type 1 events preceding Type 2 or 3 events (**Fig. 7A-B**). For instance, across participants, we found a significant deflection in the Type 1-triggered LFP after the Type 1 events (after normalizing relative to 0.5 sec before the fast event) across participants (p<0.05, false discovery rate controlled; N=29; **Supplemental Fig. 17**).

Calculating the cross-covariance of the timing of the Type 2 and 3 peaks with the Type 1 events for the baseline recordings only, we found small, but prominent, peaks in the cross-covariances with Type 1 events preceding Type 2 and Type 3 events, often by ~10 ms (**Fig. 7C**). The small cross-covariance peak was present also between the Type 2 to Type 3, with a distribution of Type 3 events preceding Type 2 events (**Fig. 7C**). However, these relative proportions were low (maxima at 0.002) which prompted us to ask whether the covariance before and after the Type 1 or Type 2 events were significant (**Fig. 7D**). We found the Type 1 covariance was significantly higher with the Type 2 and Type 3 events across participants for the 50 ms after the Type 1 event than before (p<0.001; Wilcoxon rank sum test; N=29; **Fig. 7D**). By contrast, the Type 2 covariance was significantly higher with the Type 3 events across participants for the 50 ms before the Type 2 event (p<0.001; Wilcoxon rank sum test; N=29; **Fig. 7D**). Another way to measure the timing difference between the events was to take the maximum time lag between Type 1 events and the Type 2 and Type 3 events for each recording and examine the count and distribution of the maximum lag. Again, we found a delayed peak around 10 ms in the maximum time lag counts from the covariance between Type 1 and Type 2 and Type 1 and Type 3 events, though this was out of 1298 total Type 1 isolated identified and repeated events, so the proportion of Type 1 events preceding Type 2 or 3 events was relatively low but was present across recordings (**Fig. 7E**). This trend likely contributed to the significant median maximum lag between Type 1 and Type 2 events (with Type 2 events following Type 1 events; p=0.0004; Wilcoxon signed rank test for significant different to zero; N=29; **Fig. 7F**).

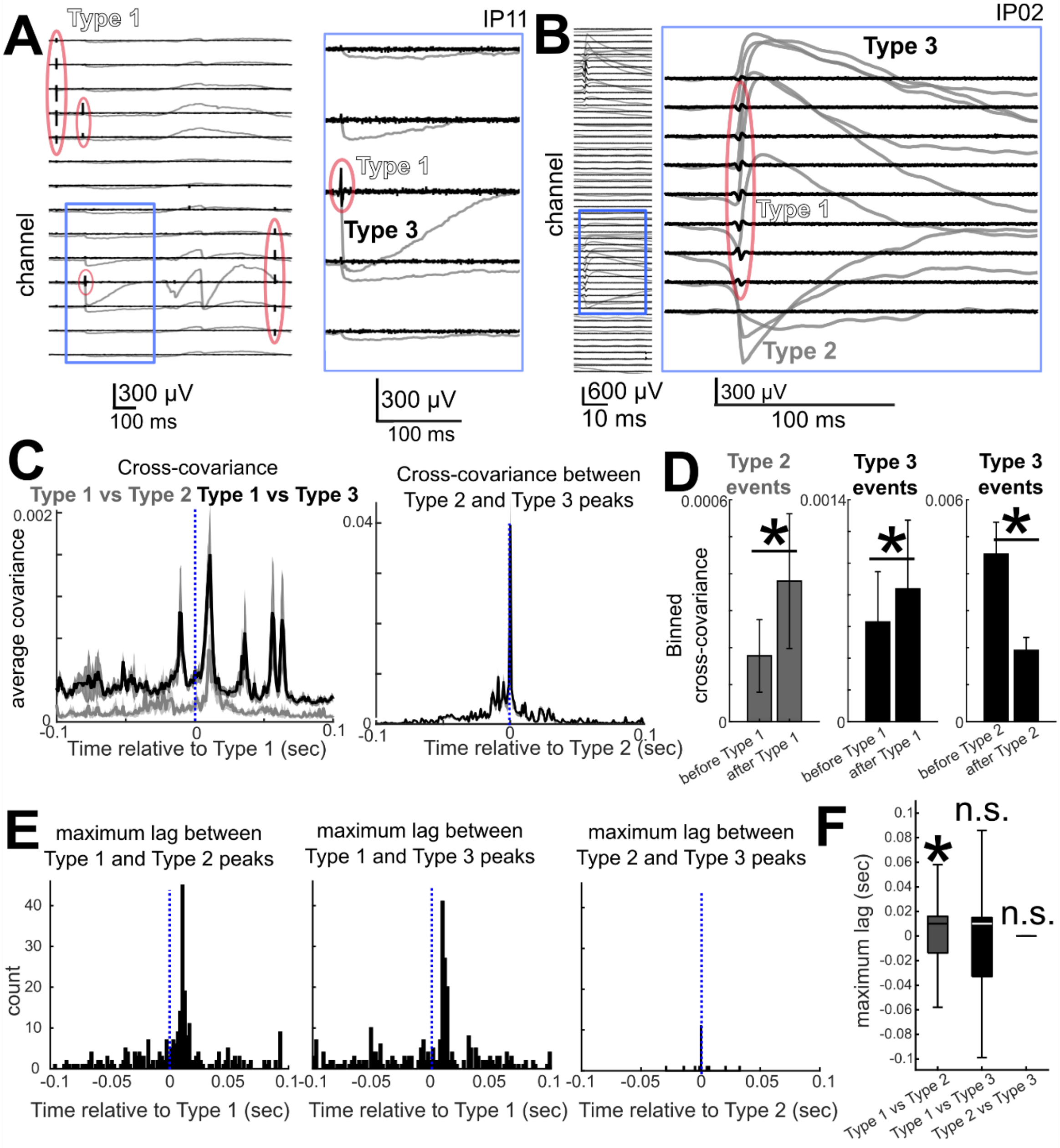

Figure 7. Relationships between Types of events. A-B. Concurrent Type 1, 2, and 3 events across participants and across channels as recorded in the high frequency range (high pass filtered data between 250 and 6000 Hz, black lines) versus the low frequency range (low pass filtered at 500 Hz, grey lines). Type 1 events are circled in red. **C.** Left: Average cross-covariance plots between Type 1 and Type 2 (grey line) and Type 3 (black line) events co-

occurring in time. Right: Average cross-covariance plots between Type 2 and Type 3 events co-occurring in time. Shaded lines are standard error. **D.** Average covariance from the 50 ms before each event versus after each event. Asterisks indicate $p<0.001$; N=29; Wilcoxon rank sum test. Error bars are s.e.m. **E**. Binned maximum time lag between Type 1 event and the Type 2 and Type 3 events for all the recordings in humans (two right plots) and the binned maximum time lag between the Type 2 and Type 3 events. **F**. Median maximum lag in covariance between Type 1 and Type 2 (grey box plot), Type 1 and Type 3 (black box plot), and Type 2 and Type 3 events with confidence bounds. Asterisk indicates distribution is significantly different to zero, $p=0.0004$; N=29. Wilcoxon signed rank test.

Discussion

A mainstay of neuroscience research, particularly in the mammalian cortex, has been the use of extracellular recordings to detect LFPs and single units – especially in layers 4 and 5 in the cortex. However, this work shows that a powerful byproduct of increased density and low impedance electrodes is not only increased access to neural activity but access to what could be other forms of neural activity otherwise not detected using penetrating metal intraparenchymal electrodes. We observed fast, repeated, localized waveforms across the recordings as well as two further types of events (Type 2 and Type 3) which were slower in waveform rise and fall times than the fast Type 1 events. With the goal of characterizing these events to determine 1) if any of these events are physiological and 2) begin to lay the groundwork for future studies into the neural substrate underlying these events, we set out to describe and test how these events change their activity through physiological manipulations while determining their relationships to underlying oscillations as well as the relationships between these events.

To exclude the possibility that these events were an artifact of the recording system and other confounds, we performed recordings in four different centers (MGH, BWH, UCSD, OHSU), in 30 patients, in mice and an NHP, and with five different physical electrophysiological setups equipped with two different recording systems (Intan and Blackrock). We were able to modulate these event types through pharmacological means, application of cold saline and, most importantly, sensory stimuli. Type 1, 2 and 3 events were selectively altered in frequency with auditory stimuli, were selectively and separately inhibited by pro-convulsant medication and cold saline and were differentially impacted by electrical stimulation. They were present in animal models as well but essentially absent in non-biological recordings (e.g. in saline and after euthanasia). Furthermore, Type 1-3 events had characteristic spatiotemporal patterns, were repeated and localized, and showed rare but statistically significant interactions between the different event types.

A concern could be that these events were a product of the manufacture and quality of the PEDOT:PSS electrodes as some electrodes had considerable failures in recording quality. However, unless we actively moved the electrode in saline to provide movement artifacts (which can be a confound in any electrode type), we did not observe the Type 1, 2, and 3 events even when we recorded over cortical V1 in a recently euthanized mouse.

A significant issue for this entire study is whether the Type 1, 2, and 3 events reflect normal brain activity or are only representative of brain tissue near tumors or areas producing abnormal activity such as epileptiform activity. Were this the case, it would still be of significant interest as a biomarker of pathology; however, there is substantial evidence that these are physiologically normal events. First, that pathological events would be induced by auditory stimuli is unlikely but possible. Second, we found these events in all patients examined regardless of their reason for their surgery or location of recording. Additionally, we observed similar events in both rodents and an NHP. Taken together, these findings strongly suggest that these surface recorded events are physiological in nature and could be found in normal tissue.

Interestingly, the Type 1, 2, and 3 events appeared as unitary occurrences with asymmetric waveforms, relatively fast kinetics and without rhythmicity, indicating that they were not part of typical ongoing oscillations. If they were part of an ongoing oscillation, then we would expect a longer-term increase in power before and after the event locked to the event onset. However, we found an increase in power in a subset of frequency bands in the event-locked spectral analyses immediately preceding the events. These power changes were highly localized in time, even for the slower Type 3 events, indicating that ongoing oscillations were not necessarily preceding the events in time and can even be inhibited following the events.

While the cellular processes underlying these events are unknown, a number of possibilities exist. One is that they reflect the activity in specific neuronal cell types present in Layer I of the cortex (Boldog et al., 2018; Gabbott, 2016; Mohan et al., 2015; Rakic and Zecevic, 2003; Zaitsev et al., 2009). This could include Cajal-Retzius cells or other relatively rare types whose cell bodies are found in upper cortical layers (Gabbott, 2016; Mohan et al., 2015; Rakic and Zecevic, 2003). There is also the possibility that these events reflect miniature inter-ictal discharges (IIDs) reflective of epileptiform activity (Curtis et al., 2012; Schevon et al., 2008, 2010). However, we observe these events in normal mice and an NHP. These events could reflect ionic flux in glial cells in upper cortical layers – although the fast kinetics makes this somewhat less likely as astrocytic waves normally occur on the time scale of seconds (Hassinger et al., 1996; Khakh and McCarthy, 2015; Kuga et al., 2011; Rouach et al., 2018; Scemes and Giaume, 2006; Takata and Hirase, 2008).

More plausible and intriguing is the possibility that these events are back-propagating dendritic action potentials (Moore et al., 2017; Robbins et al., 2013; Stuart and Spruston, 2015) or even dendritic calcium spikes (Suzuki and Larkum, 2017). A similar type of event has been reported using fine electrodes in freely behaving rats, specifically recording what could be dendritic action potentials using tetrodes following the formation of a glial sheath to increase the contact between neural dendrites and the fine wires (Moore et al., 2017). The waveform shapes of extracellular dendritic action potentials as reported using this approach were very similar to the Type 2 events described here, though the reported dendritic action potentials were shorter (duration ~5-10 ms) they did have similar voltage range (~.5-1 mV). One or both of Type 2 and 3 events could also be indicative of localized calcium spikes in the apical tufts of pyramidal neurons from deeper layers (Golding et al., 2018; Ross, 2015; Suzuki and Larkum, 2017). Similar time courses and waveforms have also been recorded from the surface of the cortex in anesthetized rats which were then verified, through optogenetics, linear probes, pharmacological manipulation, and a number of tools including calcium imaging, to be dendritic calcium spikes from layer 2/3 or layer 5 pyramidal neurons (Suzuki and Larkum, 2017). These results open up the possibility that we could be recording these events with the use of high density surface electrodes.

In addition to the new types of activity these electrodes could be detecting, PEDOT:PSS microelectrodes record Type 1 waveforms which were within the range of extracellular action potentials dynamics despite being on the cortical surface. However, Type 1 repeated waveform events also included waveforms with very narrow potentials, some with a triphasic appearance and some which were relatively large compared to previously recorded action potentials. With their short duration, these events more closely resemble recordings made of action potentials in axons (Bakkum et al., 2013; Barry, 2015; Jun et al., 2017; Stuart and Spruston, 2015). In this scenario, these events may be capturing activity in unmyelinated axons in the uppermost cortical layers (Mohan et al., 2015). Supporting this notion, to some extent, was the observed relationship whereby the fast Type 1's preceded some of the Type 2 and 3 events implying that the fast Type 1 events are presynaptic axon potentials while the slower events are a post-synaptic consequence. These possibilities may be the reason we are finding colocalized, though time delayed co-occurrence between the Type 1 and Type 2 and 3 events. While the colocalization was rare across recordings, the timing relationships were significant. It should be noted that primate pyramidal neurons have been shown to produce fast (or 'thin') spikes compared to non-primate species (Vigneswaran et al., 2011). The different waveform shapes for the fast events we identified could also be representative of different neuronal subclasses (Bartho et al., 2004; Chan et al., 2014; Trainito et al., 2019; Vigneswaran et al., 2011), though further investigation is required.

Calcium imaging and voltage imaging approaches in animal models may be necessary to explore these events in more detail. Yet, we would still not be able to fully determine the production mechanisms of these events without employing multiple modalities at once or in the same preparation to gather a more complete picture of brain dynamics in non-human preparations (Abdelfattah et al., 2019; Adam et al., 2019; Harvey et al., 2009). For this reason, we would suggest using the information gained in this study to look at equivalent preparations, in awake un-anesthetized animals, where one could examine the calcium dynamics (Suzuki and Larkum, 2017), intracellular changes (Abdelfattah et al., 2019; Harvey et al., 2009), introduce pharmacological interventions (Suzuki and Larkum, 2017), and possibly manipulate expression patterns and activation of relevant cell subtypes (Abdelfattah et al., 2019). For instance, it would be interesting if the selective increase in Type 3 events with word-like sounds over white noise was due to cell subtypes or local network dynamics. In the case of electrical stimulation, the fact that the Type 1 events have an inverse response profile to Type 2 and 3 events could speak to the involvement of different cell subpopulations or local versus distant response profiles and it would be fascinating to test this paradigm with recently developed voltage dynamic imaging approaches such as Voltron (Abdelfattah et al., 2019), particularly under a wide range of conditions while probing and manipulating the pre- and post synaptic elements and activity patterns. Thus, our results provide a foundation for future investigations into the underlying circuit activity not just at the single cell level but the intermediate range of activity that most networks, cognitive processing, and neural underpinnings of behavior operate: between the edge of the lone cell and the whole brain.

Acknowledgements

We would like to thank Yangling Chou, Erica Johnson, Milan Halgren, Alexandra O'Donnell, Melissa Murphy, Aaron Tripp, Alex Zhang, and Gavin Belok for help in data collection and, of course, the patients for their willingness to participate in this research. This research was sponsored by the U.S. Army Research Office and Defense Advanced Research Projects Agency under Cooperative Agreement Number W911NF-14-2-0045. In addition, other support included National Institutes of Health under Award Number 1F32MH120886 to DRC, ECOR and K24-NS088568 to SSC, Tiny Blue Dot Foundation to SSC and ACP, and by an NSF-CAREER award #1351980, NSF CMMI award #1728497, BRAIN Initiative R01MH111359 to AD, NSF-ECCS EAGER award #1743694 to SAD, and NIH (NEI R01-EY029022 / EY023651 and NINDS U01-NS099700) and by the Dept. of Defense / CDMRP (VR170089) to SBR, SWL, and SIF. The views and conclusions contained in this document are those of the authors and do not represent the official policies, either expressed or implied, of the funding sources.

Author Contributions

Conceptualization, A.C.P., J.C.Y., S.S.C., S.A.D. Methodology, J.H., M.G., A.C.P., J.C.Y., S.S.C., S.A.D. Formal analysis, A.C.P., J.C.Y., D.J.S. Investigation, A.C.P., J.C.Y., D.R.C., N.R., K.K., S.B.R., S.W.L., D.M., S.I.F., P.S.J., B.V.N., S.B-H., A.M.T.R., D.S., D.P.C., Z.M.W., G.R.C., S.A.D., S.S.C. Resources, S.A.D., S.S.C., S.I.F, S.W.L., S.H.L., M.G., Y.G.R., H.O., L.H. Data curation, A.C.P., D.J.S., J.C.Y. Writing, A.C.P., J.C.Y., S.S.C., S.A.D., D.P.C., Z.M.W., S.B.R., N.R., A.D., D.J.S., D.R.C., J.L., G.R.C. Visualization, A.C.P., D.J.S. Supervision, S.A.D., S.S.C. Project administration, A.C.P., J.C.Y., D.R.C., S.A.D., S.S.C. Funding acquisition, S.A.D., S.S.C., S.I.F., S.W.L.

Declaration of Interests

The authors declare no competing interests.

References

Abdelfattah, A.S., Kawashima, T., Singh, A., Novak, O., Liu, H., Shuai, Y., Huang, Y.-C., Campagnola, L., Seeman, S.C., Yu, J., et al. (2019). Bright and photostable chemigenetic indicators for extended in vivo voltage imaging. *Science* **365**, 699–704.

Adam, Y., Kim, J.J., Lou, S., Zhao, Y., Xie, M.E., Brinks, D., Wu, H., Mostajo-radji, M.A., Kheifets, S., Parot, V., et al. (2019). Voltage imaging and optogenetics reveal behaviour-dependent changes in hippocampal dynamics. *Nature* **569**, 413–417.

Anastassiou, C.A., Perin, R., Buzsáki, G., Markram, H., and Koch, C. (2015). Cell type- and activity-dependent extracellular correlates of intracellular spiking. *J. Neurophysiol.* **114**, 608–23.

Bakkum, D.J., Frey, U., Radivojevic, M., Russell, T.L., Müller, J., Fiscella, M., Takahashi, H., and Hierlemann, A. (2013).

Berger, M.S., and Ojemann, G.A. (1992). Intraoperative brain mapping techniques in neuro-oncology. *Stereotact. Funct. Neurosurg.* **58**, 153–161.

Boldog, E., Bakken, T.E., Hodge, R.D., Novotny, M., Aevermann, B.D., Baka, J., Bordé, S., Close, J.L., Diez-Fuertes, F., Ding, S.L., et al. (2018). Transcriptomic and morphophysiological evidence for a specialized human cortical GABAergic cell type. *Nat. Neurosci.* **21**, 1185–1195.

Borchers, S., Himmelbach, M., Logothetis, N., and Karnath, H. (2012). Direct electrical stimulation of human cortex — the gold standard for mapping brain functions? *Nat. Rev. Neurosci.* **13**, 63–70.

Cellot, G., Lagonegro, P., Tarabella, G., Scaini, D., Fabbri, F., Iannotta, S., Prato, M., Salviati, G., and Ballerini, L. (2016). PEDOT:PSS interfaces support the development of neuronal synaptic networks with reduced neuroglia response in vitro. *Front. Neurosci. 9*, 1–11.

Chan, A.M., Dykstra, A.R., Jayaram, V., Leonard, M.K., Travis, K.E., Gygi, B., Baker, J.M., Eskandar, E., Hochberg, L.R., Halgren, E., et al. (2014). Speech-specific tuning of neurons in human superior temporal gyrus. *Cereb. Cortex* **24**, 2679–2693.

Curtis, M. D., Jefferys, J. G. R. &., and Avoli, M. (2012). Interictal Epileptiform Discharges in Partial Epilepsy: Complex Neurobiological Mechanisms Based on Experimental and Clinical

Evidence. In *Jasper's Basic Mechanisms of the Epilepsies* 1–24 (Bethesda (MD): National Center for Biotechnology Information (US), 2012), pp. 1–24.

Fried, I., Mukamel, R., and Kreiman, G. (2011). Internally Generated Preactivation of Single Neurons in Human Medial Frontal Cortex Predicts Volition. *Neuron* **69**, 548–562.

Gabbott, P.L.A. (2016). "Subpial Fan Cell" — A Class of Calretinin Neuron in Layer 1 of Adult Monkey Prefrontal Cortex. *Front. Neuroanat.* **10**, 1–29.

Ganji, M., Kaestner, E., Hermiz, J., Rogers, N., Tanaka, A., Cleary, D., Lee, S.H., Snider, J., Halgren, M., Cosgrove, G.R., et al. (2017a). Development and Translation of PEDOT:PSS Microelectrodes for Intraoperative Monitoring. Adv. Funct. Mater. 28, 1700232.

Ganji, M., Atsunori, T., Vikash, G., Eric, H., and Dayeh, S.A. (2017b). Scaling Effects on the Electrochemical Stimulation Performance of Au, Pt, and PEDOT:PSS Electrocorticography Arrays. Adv. Funct. Mater. 27, 1703019.Golding, N.L., Jung, H., Mickus, T., and Spruston, N. (2018). Dendritic Calcium Spike Initiation and Repolarization Are Controlled by Distinct Potassium Channel Subtypes in CA1 Pyramidal Neurons. *J. Neurosci.* **19**, 8789–8798.

Hamilton, F., Berry, T., and Sauer, T. (2018). Tracking intracellular dynamics through extracellular measurements. *PLoS ONE* **13**, 1–13.

Harvey, C.D., Collman, F., Dombeck, D. a, and Tank, D.W. (2009). Intracellular dynamics of hippocampal place cells during virtual navigation. *Nature* **461**, 941–6.

Hassinger, T.D., Guthrie, P.B., Atkinson, P.B., Bennett, M.V.L., and Kater, S.B. (1996). An extracellular signaling component in propagation of astrocytic. *Proc. Natl. Acad. Sci.* **93**, 13268–13273.

Hermiz, J. (2018). Electrocorticography on the Micron Scale: Single Units and Enhanced Neural State Estimation (Diss. UC San Diego).

Hermiz, J., Rogers, N., Kaestner, E., Ganji, M., Cleary, D., Snider, J., Barba, D., Dayeh, S., Halgren, E., and Gilja, V. (2016). A clinic compatible, open source electrophysiology system. In (1998). *38th Annual International Conference of the IEEE Engineering in Medicine and Biology Society (EMBC),* pp. 4511–4514 (2016). doi:10.1109/EMBC.2016.7591730 .

Holmes, C.J., Hoge, R., Collins, L., Woods, R., Toga, A.W., and Evans, A.C. (1998). Enhancement of MR Images Using Registration for Signal Averaging. *J. Comput. Assist. Tomogr.* **22**, 324–333.

Janca, R., Jezdik, P., Cmejla, R., Tomasek, M., Worrell, G.A., Stead, M., Wagenaar, J., Jefferys, J.G.R., Krsek, P., Komarek, V., et al. (2015). Detection of Interictal Epileptiform Discharges Using Signal Envelope Distribution Modelling: Application to Epileptic and Non-Epileptic Intracranial Recordings. *Brain Topogr.* **28**, 172–183 (2015).

Jun, J.J., Steinmetz, N.A., Siegle, J.H., Denman, D.J., Bauza, M., Barbarits, B., Lee, A.K., Anastassiou, C.A., Andrei, A., Aydın, Ç., et al. (2017). Fully integrated silicon probes for high-density recording of neural activity. *Nature* **551**, 232.

Kaestner, E. (2018). *A Motor Theory of Reading: The interaction of visual and auditory language*. PhD Thesis.

Kaiju, T., Doi, K., Yokota, M., Watanabe, K., Inoue, M., Ando, H., Takahashi, K., Yoshida, F., Hirata, M., and Suzuki, T. (2017). High Spatiotemporal Resolution ECoG Recording of Somatosensory Evoked Potentials with Flexible Micro-Electrode Arrays. *Front. Neural Circuits* **11**, 1–13.

Kawaguchi, M., Shimizu, K., Karasawa, J., and Furuya, H. (1996). Intraoperative Myogenic Motor Evoked Potentials Induced by Direct Electrical Stimulation of the Exposed Motor Cortex Under Isoflurane and Sevoflurane. *Anesth. Analg.* **82**, 593–599.

Keller, C.J., Truccolo, W., Gale, J.T., Eskandar, E., Thesen, T., Carlson, C., Devinsky, O., Kuzniecky, R., Doyle, W.K., Madsen, J.R., et al. (2010). Heterogeneous neuronal firing patterns during interictal epileptiform discharges in the human cortex. *Brain* **133**, 1668–1681.

Khakh, B.S., and McCarthy, K.D. (2015). Astrocyte calcium signaling: From observations to functions and the challenges therein. *Cold Spring Harb. Perspect. Biol. 7*, 1–18.

Khodagholy, D., Gelinas, J.N., Thesen, T., Doyle, W., Malliaras, G.G., and Buzsáki, G. (2015). NeuroGrid: recording action potentials from the surface of the brain. *Nat. Neurosci.* **18**, 310–315.

Khodagholy, D., Gelinas, J.N., Zhao, Z., Yeh, M., Long, M., Greenlee, J.D., Doyle, W., Devinsky, O., and Buzsáki, G. (2016). Organic electronics for high-resolution electrocorticography of the human brain. *Sci. Adv.* **2**, e1601027.

Khodagholy, D., Gelinas, J.N., and Buzsáki, G. (2017). Learning-enhanced coupling between ripple oscillations in association cortices and hippocampus. *Science* **372**, 369–372.

Kuga, N., Sasaki, T., Takahara, Y., Matsuki, N., and Ikegaya, Y. (2011). Large-Scale Calcium Waves Traveling through Astrocytic Networks In Vivo. *J. Neurosci.* **31**, 2607–2614.

Mehran, G., Atsunori, T., Vikash, G., Eric, H., and Dayeh, S.A. (2017). Scaling Effects on the Electrochemical Stimulation Performance of Au, Pt, and PEDOT:PSS Electrocorticography Arrays. *Adv. Funct. Mater.* **27**, 1703019.

Mohan, H., Verhoog, M.B., Doreswamy, K.K., Eyal, G., Aardse, R., Lodder, B.N., Goriounova, N.A., Asamoah, B., B. Brakspear, A.B.C., Groot, C., et al. (2015). Dendritic and axonal architecture of individual pyramidal neurons across layers of adult human neocortex. *Cereb. Cortex* **25**, 4839–4853.

Moore, J.J., Ravassard, P.M., Ho, D., Acharya, L., Kees, A.L., Vuong, C., and Mehta, M.R. (2017). Dynamics of cortical dendritic membrane potential and spikes in freely behaving rats. *Science* **355**, eaaj1497.

Mueller, W.M., and Morris, G.L. (1993). Intraoperative and Extraoperative Identification of Eloquent Brain Using Stimulation Mapping. *Neurosurg. Clin. N. Am.* **4**, 217–222.

Oostenveld, R., Fries, P., Maris, E. &., and Schoffelen, J.-M. (2011). FieldTrip: Open source software for advanced analysis of MEG, EEG, and invasive electrophysiological data. *Comput. Intell. Neurosci.* **2011**, 156869.

Ossmy, O., Fried, I., and Mukamel, R. (2015). Decoding speech perception from single cell activity in humans. *NeuroImage* **117**, 151–159.

Pachitariu, M., Steinmetz, N., Kadir, S., Carandini, M., and Harris, K. (2016). Fast and accurate spike sorting of high-channel count probes with KiloSort. *Adv. Neural Inf. Process. Syst.* **2016**, 1–9.

Paxinos, G., and Franklin, K.B.J. (2001). The mouse brain in stereotaxic coordinates (Academic Press).

Peled, N., Gholipour, T., Paulk, A.C., Felsenstein, O., Dougherty, D.D., Widge, A.S., Eskandar, E.N., Cash, S.S., Hamalainen, M.S., and Stufflebeam, S.M. (2017). Invasive Electrodes Identification and Labeling. *GitHub Repos.* **https://github.com/pelednoam/ieil**.

Postelnicu, G., Zöllei, L., and Fischl, B. (2009). Combined Volumetric and Surface Registration. *October* **28**, 508–522.

Rakic, S., and Zecevic, N. (2003). Emerging complexity of layer I in human cerebral cortex. *Cereb. Cortex* **13**, 1072–1083.

Reuter, M., Rosas, H.D., and Fischl, B. (2010). Highly Accurate Inverse Consistent Registration: A Robust Approach. *NeuroImage* **53**, 1181–1196.

Reuter, M., Schmansky, N.J., Rosas, H.D., and Fischl, B. (2012). Within-Subject Template Estimation for Unbiased Longitudinal Image Analysis. *NeuroImage* **61**, 1402–1418.

Rivnay, J., Inal, S., Collins, B.A., Sessolo, M., Stavrinidou, E., Strakosas, X., Tassone, C., Delongchamp, D.M., and Malliaras, G.G. (2016). Structural control of mixed ionic and electronic transport in conducting polymers. *Nat. Commun.* **7**, 11287.

Robbins, A.A., Fox, S.E., Holmes, G.L., Scott, R.C., and Barry, J.M. (2013). Short duration waveforms recorded extracellularly from freely moving rats are representative of axonal activity. *Front. Neural Circuits* **7**.

Ross, W.N. (2015). Understanding calcium waves and sparks in central neurons. *Nat Rev Neurosci.* **13**, 157–168.

Rouach, N., Dao Duc, K., Sibille, J., Holcman, D., Holcman, D., and Rouach, N. (2018). Dynamics of ion fluxes between neurons, astrocytes and the extracellular space during neurotransmission. BioRxiv *4,* 1–18.

Scemes, E., and Giaume, C. (2006). Astrocyte Calcium Waves: What they are and what they do. *Glia* **54**, 716–725.

Schevon, C.A., Ng, S.K., Cappell, J., Goodman, R.R., McKhann, G., Waziri, A., Branner, A., Sosunov, A., Schroeder, C.E., and Emerson, R.G. (2008). Microphysiology of epileptiform activity in human neocortex. *J. Clin. Neurophysiol.* **25**, 321–330.

Schevon, C.A., Goodman, R.R., McKhann, G., and Emerson, R.G. (2010). Propagation of epileptiform activity on a submillimeter scale. *J. Clin. Neurophysiol.* **27**, 406–411.

Sessolo, M., Khodagholy, D., Rivnay, J., Maddalena, F., Gleyzes, M., Steidl, E., Buisson, B., and Malliaras, G.G. (2013). Easy-to-Fabricate Conducting Polymer Microelectrode Arrays. *Adv. Mater.* **25**, 2135–2139.

Siegle, J.H., López, A.C., Patel, Y.A., Abramov, K., Ohayon, S., and Voigts, J. (2017). Open Ephys: An open-source, plugin-based platform for multichannel electrophysiology. *J. Neural Eng. 14*.

Stuart, G.J., and Spruston, N. (2015). Dendritic integration: 60 years of progress. *Nat. Neurosci.* **18**, 1713–1721.

Suzuki, M., and Larkum, M.E. (2017). Dendritic calcium spikes are clearly detectable at the cortical surface /631/378 /631/443 article. *Nat. Commun. 8,* 1–10.

Takata, N., and Hirase, H. (2008). Cortical layer 1 and layer 2/3 astrocytes exhibit distinct calcium dynamics in vivo. *PLoS ONE* **3**.

Trainito, C., Nicolai, C.V., Miller, E.K., and Siegel, M. (2019). Extracellular spike waveform dissociates four functionally distinct cell classes in primate cortex. BioRxiv 1–36.

Travis, K.E., Leonard, M.K., Chan, A.M., Torres, C., Sizemore, M.L., Qu, Z., Eskandar, E., Dale, A.M., Elman, J.L., Cash, S.S., et al. (2013). Independence of early speech processing from word meaning. *Cereb. Cortex* **23**, 2370–2379.

Uguz, I., Ganji, M., Adel, H., Atsunori, T., Inal, S., Ahmed, Y., Owens, R.M., Quilichini, P.P., Ghestem, A., Christophe, B., et al. (2016). Autoclave Sterilization of PEDOT:PSS Electrophysiology Devices. *Adv. Healthc. Mater.* **5**, 3094–3098.

Vigneswaran, G., Kraskov, A., and Lemon, R.N. (2011). Large Identified Pyramidal Cells in Macaque Motor and Premotor Cortex Exhibit “Thin Spikes”: Implications for Cell Type Classification. *J. Neurosci.* **31**, 14235–14242.

Viventi, J., Kim, D.H., Vigeland, L., Frechette, E.S., Blanco, J.A., Kim, Y.S., Avrin, A.E., Tiruvadi, V.R., Hwang, S.W., Vanleer, A.C., et al. (2011). Flexible, foldable, actively multiplexed, high-density electrode array for mapping brain activity in vivo. *Nat. Neurosci.* **14**, 1599–1605.

Wilks, S.J., Woolley, A.J., Ouyang, L., Martin, D.C., and Otto, K.J. (2011). In vivo polymerization of poly(3,4-ethylenedioxythiophene) (PEDOT) in rodent cerebral cortex. (In 2011). Annual International Conference of the IEEE Engineering in Medicine and Biology Society, pp. 5412–5415.

Yildirim, M., Sugihara, H., So, P.T.C., and Sur, M. (2019). Functional imaging of visual cortical layers and subplate in awake mice with optimized three-photon microscopy. *Nat. Commun. 10*.

Zaitsev, A.V., Povysheva, N.V., Gonzalez-Burgos, G., Rotaru, D., Fish, K.N., Krimer, L.S., and Lewis, D.A. (2009). Interneuron diversity in layers 2-3 of monkey prefrontal cortex. *Cereb. Cortex* **19**, 1597–1615.

Methods

Human Participants

Human recordings during neural stimulation were acquired with 30 participants (mean=38.7 years old, ranging from 22 to 62; 16 females; all but 5 individuals right handed **Supplemental Tables 1-2**) who were scheduled for surgical resection of cortical tissue as a result of tumor or epilepsy at Massachusetts General Hospital (MGH), Brigham and Women's Hospital (BWH), University of California San Diego (UCSD), and Oregon Health and Science University (OHSU). Patients were already scheduled for a craniotomy for concurrent clinical intraoperative neurophysiological monitoring or testing for mapping motor, language, and sensory regions and removal of tissue.

In some cases (N=8), pro-convulsant medications (methohexital or alfentanil) were given intravenously to the participants in the process of clinically mapping the putative seizure focus while recording with the clinical electrodes. This choice was made by the clinical team. In another subset of cases (N=7), cold saline was applied for the purposes of reducing overactive tissue clinically or to determine how underlying activity changes with a change in temperature. Finally, with some participants (N=8), repetitive sounds (1 sec between each sound) were played back to the participants via a speaker in the operating room (OR; N=2) or via headphones to the participant (N=6) using Presentation software (Neurobehavioral Systems) to determine if there was an auditory response to the sounds. The different types of sounds were either real words, nonsense syllables which were not English words, and noise-vocoded sounds (which involved a white noise convolution of the real words) (Hermiz et al., 2018; Kaestner, 2018; Travis et al., 2013).

Following the surgery, the preoperative T1-weighted MRI was reconstructed using FreeSurfer scripts (Desikan et al., 2006; Reuter et al., 2010, 2012) (http://surfer.nmr.mgh.harvard.edu). The reconstructions were then aligned to images during surgery using blender software (https://www.blender.org/) and MMVT (Dykstra et al., 2012; Felsenstein and Peled, 2017; Holmes et al., 1998; Peled et al., 2017). The method involved projecting the image from the surgery which included the craniotomy and the PEDOT electrode onto the patient's reconstructed brain using blender and then placing a 3D model of the PEDOT electrode array on that location similar to other coregistration approaches (Dykstra et al., 2012; Holmes et al., 1998; Postelnicu et al., 2009) (**Fig. 1; Supplemental Fig. 1-3**; **Fig. 1; Supplemental Fig. 1-3**).

Non-Human Primate Surgical Details and Recording Methods

Experimental procedures on one rhesus macaque were carried out according to the Guide to the Care and Use of Laboratory Animals. All efforts were made to minimize discomfort, and the Institutional Animal Care and Use Committee at the Massachusetts General Hospital monitored care and approved all procedures.

Intraoperative, intracranial neurophysiology recordings were acquired from one adult male rhesus macaque (*Macaca mulatta*, age 14). The macaque was placed under general endotracheal anesthesia (isoflurane) and placed into a stereotactic frame (Kopf; Kujunga, CA). A craniotomy over the visual cortex were performed using standard anatomic landmarks, and cortex was carefully exposed. Using gyral anatomy and vasculature over V1 versus V4 (**Figure 4**), the V4 area was identified visually and a PEDOT electrode was placed over the region. Signals were recorded using the ORH128 Intan Recording System (Hermiz, 2018; Hermiz et al., 2016). The data was acquired at 30 KHz and filtered by default Intan setting with cutoffs 1 Hz to 7.5 kHz and using OpenEphys acquisition graphic-user interface software (Siegle et al., 2017; http://www.open-ephys.org/), with the impedance tests of the electrodes during the experiments carried out using the Intan RHD2000 software from Intan Technologies (Los Angeles, CA). Data was extracted and processed using MATLAB (Mathworks, Natick, MA).

Area V1 Mouse Surgical Details and Recording Methods

The care and use of mice (2-6 months old; C57BL/6J; Jackson Laboratory, Bar Harbor, ME) followed all federal and institutional guidelines, and the Institutional Animal Care and Use Committees of the Massachusetts General Hospital. Mice were deeply anaesthetized with a cocktail of injected ketamine hydrochloride (100 mg/kg intraperitoneal injection) and xylazine (10 mg/kg i.p. injection; N=1) or isoflurane administered as a gas prior and during the start of surgery (N=2). In the mouse given ketamine, additional ketamine (1/10 initial dose) was supplemented every 30 min to maintain the plane of anesthesia.

Anesthetized mice were placed into a stereotaxic frame (Narishige, Japan) for the craniotomy as well as all subsequent testing. A heating blanket on the floor of the frame was used to maintain body temperature at 37°C. A craniotomy was performed on 4.5 mm x 4.5 mm area around the primary visual cortex (V1) defined by a stereotaxic coordinate (AP : -3.8, ML: -2 mm; (Paxinos and Franklin, 2001)). A small craniotomy was made in the skull, the PEDOT:PSS array was placed over the exposed visual cortex over intact dura. Once the PEDOT:PSS array was positioned on V1, neural signals were recorded using the ORH128 Intan Recording System, acquiring data at 30 KHz and filtered by the default Intan setting (cutoffs 1 Hz to 7.5 kHz). Data was extracted and processed using MATLAB.

Barrel Cortex Mouse Surgical Details and Recording Methods

ICR mice weighing 25-35 g were used in the experiments. All procedures were in accordance with a protocol approved by the Institutional Animal Care and Use Committees of UC San Diego (protocol S07360). The mice were anesthetized with isoflurane, a femoral artery was catheterized to allow recording of blood pressure, and a tracheotomy was performed for ventilation of the mice. A metal headpost was fixed to the skull using dental acrylic, a craniotomy and durotomy were performed over the right whisker barrel and surrounding cortex. The exposure was surrounded by a dental acrylic well in order to keep it filled with artificial CSF until the electrode array was placed. The exposure was dried prior to the electrode placement, and then once the array was implanted it was covered with 0.7% agarose in artificial CSF. The electrodes arrays used were arranged in square grids with 0.2 mm spacing, and 50 micron diameter contacts. The reference electrode was silver-chloride ball placed between muscle tissue exposed for the craniotomy. Prior to recording the mice were administered pancuronium and artificially ventilated, and prior to stimulus trials the mice were switched from isoflurane to alpha-chloralose anesthesia. Whisker flick stimuli were presented every 2 seconds. Neural signals were recorded at 20 kHz using an Intan recording system.

Ethics statement

All patients voluntarily participated after fully informed consent according to NIH guidelines as monitored by the Partners Institutional Review Board (IRB) which provides coverage for Massachusetts General Hospital (MGH) and Brigham and Women’s Hospital (BWH), by the UC San Diego Health IRB which provides coverage for University of California San Diego (UCSD), and the Oregon Health Sciences University IRB which provides coverage for the Oregon Health Sciences University (OHSU). Participants were informed that participation in the experiment would not alter their clinical treatment in any way, and that they could withdraw at any time without jeopardizing their clinical care.

PEDOT:PSS electrode Device Fabrication

The fabrication of the PEDOT:PSS device is similar to previously established protocols with slight modifications as noted below (Ganji et al., 2017a, 2017b; Uguz et al., 2016). Si wafers in batches of 6 wafers were used as substrate carriers for deposition of parylene C layers. Following substrate cleaning, the diluted Micro-90 (0.1%) – an anti-adhesion layer – was spun-cast at 1300 rpm on the substrate and an NR9-6000PY negative resist was used for metal electrode definition on the parylene C layers. O_2 plasma (Plasma Etch PE100) was applied for 2 min (150W RF power, 5 sccm O_2) for descum step to remove residual photoresist in patterned regions prior to the evaporation of a 15 nm Cr adhesion layer and a 100 nm Au contact layer on top of the 4μm thick parylene C layer (epidural mouse recording) or 10μm thick parylene C layer (subdural recordings for mouse, NHP, and humans). After lift-off, an O_2 plasma (Plasma Etch PE100) was applied for 2 min (150W RF power, 5 sccm O_2) to activate the surface of parylene-C for enhancing the adhesion of the subsequent 2 μm thick encapsulating parylene C layer. Another higher concentrated Micro-90 (1% as opposed to 0.1% for the first layer) layer was spun cast and a third parylene-C layer (≈ 1.9–2.5 μm) was deposited as sacrificial layer. To define the patterns on electrode sites, a 10 μm thick 2010 SU-8 photoresist layer was exposed and developed using Karl Suss MA6 mask aligner and SU8 developer. Prior to PEDOT:PSS deposition, O_2 plasma (Oxford Plasmalab 80, 200 W RF power, 32 min) was used to etch the openings in the third and second parylene-C layers all the way to the contact sites. Additionally, a hole at the center of the circular array was etched through all parylene-C layers. The remainder of the fabrication process remained essentially the same as previously reported (Ganji et al., 2017; Rivnay et al., 2016; Uguz et al., 2016).

Three different electrode designs were used. One electrode type involved 2-columns of 64-channel 20 µm diameter contact sites with 50 µm center to center pitch between adjacent contacts, which we call the 50 µm pitch 2-column grid (N=23; **Fig. 1; Supplemental Fig. 1-2**). A second array had the same material make-up but the center-to-center pitch was 800 µm, which we call the 800 µm pitch 2-column grid (N=1; **Supplemental Fig. 3**). A third array was a 128-channel grid with concentric rings at varying distances between each electrode site, which we call the circular grid ~4 mm in diameter (N=6; **Supplemental Fig. 3**). Finally, one array was used while recording over the mouse barrel cortex which was a square grid of 32 channels (**Supplemental Fig. 3**).

Data Acquisition

Human intracranial recordings in the OR from the PEDOT:PSS electrodes were made using a custom Intan recording system with a sampling rate of either 20 kHz or 30 kHz (filtered from 1 Hz to 7500 Hz to reduce aliasing; Intan Corporation, Los Angeles, CA). During acquisition, recordings were referenced to sterile ground and reference electrodes (Medtronic) placed in nearby muscle tissue as deemed safe by the neurosurgeon. After the electrode array was laid on tissue and the grounds placed, we tested impedances using the Intan system using the RHD2000 series software (Intan Corp.). In most cases, we used OpenEphys (Siegle et al., 2017), an open-source software which allowed us to save and visualize activity across all 128 channels as well as the analog input. Trigger signals produced by a custom MATLAB program indicating the hour, minute, and second were additionally sent to both the analog input for the Intan system as well as to the TRIG input to the clinical Quantum system (Natus) which was acquiring the concurrent clinical electrode recordings. The clinical Quantum system recorded neural activity at either 4096 Hz (at MGH) or 512 Hz (at BWH). At UCSD and OHSU, we recorded neural activity using the PEDOT:PSS electrode only. To test whether activity we observed was due to the Intan system, we also recorded neural PEDOT activity using a second recording system with a sampling rate of 30 kHz using a high impedance headstage and amplifiers input to a Neural Signal Processor (Blackrock Microsystems, USA). Two PEDOT electrodes (one connected to the Intan system and the other to the Blackrock system) were used in the same case for simultaneous recording for a side-by-side comparison (**Supplemental Fig. 3**).

Saline Recordings

While in the OR in a subset of cases (N=6), we performed several minutes of saline bath recordings before and after recording from the brain using the same equipment and electrodes as used in the neural recordings (**Supplemental Fig. 8-10**). For all comparisons, we performed the same analyses and classification steps as listed below on these saline tests to determine if we could observe the same events as identifying in the brain OR recordings. In two cases, we purposefully moved the electrode in the saline to reproduce some of the same movements observed in the case (**Supplemental Fig. 8**).

Electrical stimulation

Electrical stimulation was performed in N=11 cases (**Supplemental Table 1-2**). In most cases, neural stimulation was carried out for clinical purposes such as performing motor or language mapping (Borchers et al., 2012; Mueller and Morris, 1993). Stimulation was either performed using a Prass Standard Monopolar Stimulating Probe (motor mapping cases, Medtronic, USA), Disposable Double Ball Tip Nerve Stimulating Probe (speech mapping cases, Caldwell, USA), or the Nicolet Cortical Stimulator for Neurosurgery (Natus Neurology Inc., Middleton, WI, USA). For the clinical stimulation mapping (N=8), trains (at 60 Hz) or pulses of stimulation of variable length (ranging from .1 to 1 sec) and amplitude (ranging from 1 to 10 mA) were delivered via a hand-held bipolar wand at different locations based on the surgical flow of the case. Research stimulation (N=4) consisted of single pulses (1 and 2 mA in amplitude, biphasic and charge balanced of 100 µsec duration for each negative and positive pulse) or train stimulation (100 Hz, 0.5 sec duration) delivered at 5 second intervals via a pair of surface clinical strip electrodes near the PEDOT:PSS electrode.

Intraoperative Video monitoring

With the patient's informed consent, we recorded video of the surgery. The video recordings were acquired by a camera set in the operating room light (Black Diamond Video). We approximated the timing of the video recordings by annotating in the test when the electrode was placed on and removed from the brain which could also be seen in the recordings. We additionally annotated the timing and location of stimulation via bipolar contacts or movements of the PEDOT:PSS electrode in the field to confirm the timing of noisy signals relative to additional experimental events. Pictures of the preparation were also taken to illustrate the electrode location (**Fig. 1**).

Data Analysis

Data analysis was performed using custom programs in MATLAB. Cross-correlation between resampled analog trigger signals was used to align the triggers between multiple systems, both between the neural data and between the audio recordings. Since the recordings were brief (4-20 minutes) and electrodes could be moved at any point, we used the video and audio recordings as well as the voltage recordings to determine periods of stable recordings.

‘Raw’ voltage signals were taken directly from the Intan recordings. LFP data were decimated to 1000Hz and demeaned relative to the entire recording. Multi-unit activity (MUA) or spike-related activity was detected by high pass filtering the signal above 250 Hz. Channels with excessive line noise, had high impedances (>100 kΩ), or which fluctuated across the voltage range were removed from the analysis. We also noted that, since these recordings are necessarily transient in the operating room, we would find some channels would become noisier during the recordings over time as others. For this reason, we performed root mean square (RMS) calculations of electrodes for the ‘quiet’ periods of time when we identified when the electrode was not being moved and when there were no visible inter-ictal discharges (IIDs) or stimulation (**Supplemental Fig. 4**). We found that, by and large, the recordings in channels that had within-range impedances also had low RMS values (around or below an RMS of 5). However, there were a subset of channels that had high RMS values (closer to an RMS of 20-50) which we removed from further analyses. These channels tended to have recordings which were unstable through time based on the fluctuations in voltage and the presence of 60 Hz noise. After excluding the recordings from one participant, 48.5 ± 23.26 % of the electrode contacts (channels) survived channel rejection criteria across patients (**Supplemental Table 2; Supplemental Fig. 4;** see **Methods**). We also identified the locations of channels which survived the rejection criteria and found that the locations good channels varied considerably across the grids (**Supplemental Fig. 5-6**) and did not correspond to amplifier bank or physical connectivity (e.g. particular cables or connectors).

Type 1 Sorting

We first sorted Type 1 waveforms from the data high pass filtered above 250 Hz using a Butterworth filter via Offline Sorter (v4, Plexon, Inc., Texas, USA). We identified unit waveforms as activity within the range of 15-500 μV with a duration between 500-1500 μsec. However, with the pitch and high density of the electrodes, we found that we were identifying too many 'units' since the putative units likely spanned multiple channels in the recording. For this reason, we used Kilosort (Pachitariu et al., 2016). Kilosort was used to isolate units while taking into account the spatial mapping of the fast waveforms. Kilosort omits spike detection and PCA and instead combines template waveforms, associated spike locations and spike times into one model. Putative units were then rejected if the template waveform looked to be artifact (such as with stimulation) or if the units had highly regular or too short inter-spike-intervals. Rejecting units with inter-spike intervals (ISIs) corresponding with 60 Hz noise or which occurred at the same time as the stimulation, we also identified the spikes in the raw and original high pass filtered data to confirm their timing and channel location. Units were rejected if they appeared to occur at the same timing as stimulation, movement, or occurred on noisy channels.

Type 2 and 3 Event Detection and Template Matching

Since other 'events' involved both short (Type 1) and long (traveling LFP wave) timescales and varied in size and directions of deflection (due to changes in voltage polarity across electrodes), we performed a first-pass visualization to detect and annotate electrode movement, stimulation, or the presence of inter-ictal discharges (IIDs) using Wonambi, a visualization tool originally used in sleep scoring (https://wonambi-python.github.io/). We rejected any time periods when the electrodes were being moved in the recording. We identified IIDs for these analyses as events of ~250 ms duration and similar to previously published IID waveforms (Curtis et al., 2012; Janca et al., 2015) but did not include those IID waveforms in the subsequent event classification analyses since we considered those events outside of the scope of the current study.

Next, we detected peaks larger than 25 µV and took 400 ms snippets of data around each event (-100 ms to 300 ms) per channel. Among those events, we then re-aligned events relative to the largest rising or falling edge (for easier comparisons across waveforms). After examining all the waveforms both singly and using PCA (**Supplemental Fig. 7**), we found we could further remove noise by performing template matching to the latter two of three main waveform types: 1) Type 1: fast repeated waveform events, detected between 250 and 6000 Hz; 2) Type 2: peaks with a sharp rise and slow fall, ~10-30 ms absolute half-peak duration, detected below 500 Hz; or 3) Type 3: peaks with a slow rise and slow fall, ~100 ms absolute half-peak duration, detected below 500 Hz. Templates were constructed from average identified waveforms across the data set based on the frequency of the events and most common waveforms identified through PCA, which included the Type 2 and 3 events. Since we were performing the template matching on the LFP, not the raw data, we would not be able to detect Type 1 using this approach. Correlations to each waveform above 0.8 were used to exclusively bin each event into one of these three types.

Another possible explanation for these events is that they result from electrical noise or some kind of mechanical artifact. To address this, we examined saline recordings performed in the operating room using the same electrodes for several minutes before and after recording from the brain in N=6 cases (**Supplemental Fig. 8-10**). In two cases, we applied movement to the saline bowl in an attempt to reproduce the waveforms observed in the neural recordings. First, the Type 1 events observed in the neural recordings were also not present in any of the saline recordings (data not shown). We either never or very rarely detected Type 2 events in any of the saline recordings, with or without movement in saline (**Supplemental Fig. 8-10**). When we moved the electrode in the saline, waveforms similar to the Type 3 events could be identified in the saline recordings, although, these were rare compared with those of the neural recordings, and the waveforms were visibly slower to rise and fall, resulting in a lower second derivative of the onset time (**Supplemental Fig. 8**), without the sharp initial rise of Type 3 waveforms observed in the neural recordings which meant that brain-recorded Type 3 waveforms had higher second derivatives around the waveform onset (**Supplemental Fig. 8-10**). Therefore, to be more stringent in our detection algorithm for the neural recordings, we added another filtering step by thresholding on the second derivative at the onset of each waveform (see **Methods**; **Supplemental Fig. 8-10**). After examining the saline recording detections and finding overlap between on brain vs in saline recordings in the waveforms following our detection approach, we found we needed to add another detection step which involved thresholding based on the second derivative at ± 50 ms around the onset of the waveform (**Supplemental Fig. 8-10**).

Even after this added waveform onset thresholding step, most Type 2 and 3 events recorded on the surface of the brain survived the thresholding per participant (**Supplemental Fig. 8**). We found that both events happened significantly more frequently on brain tissue than in saline (p=0.0038; Kruskal-Wallis multiple comparison test; **Supplemental Fig. 10**), with a sum total of 59 Type 2 events and 854 Type 3 events across nine saline recordings and over 29 minutes versus 3,553 Type 2 events and 33,608 Type 3 events over brain tissue using the same electrodes over the same amount of time. Additionally, we found that 90% of events in saline spanned a single channel, with only 6 Type 2 events and 77 Type 3 events spanning multiple channels using our spatial extent detection window over a total period of time of 29 minutes (**Supplemental Fig. 10,** see **Methods**).

After this additional filtering step, the Type 2 and 3 classifications of LFP events were then mapped to the recordings in time to determine if they vary in frequency, size, and temporal dynamics with the introduction of auditory stimuli, pro-convulsant medication, cold saline, or electrical stimulation. Within these categories, we quantified their frequency in time as the inter-event interval (IEI) and the absolute amplitudes of the voltage deflections from baseline. We examined the rise and fall times relative to the peaks by quantifying the RC time constants $\tau_{\text{rise time}}$ and $\tau_{\text{fall time}}$ as in the following equation: $\Delta V = (V_{\text{final}} - V_{\text{start}})*(1\text{-}1/e\text{^}(\text{time}/\ \tau))$, where $\tau_{\text{rise time}}$ was calculated as time it took for the voltage to reach 0.63 of the maximum peak and $\tau_{\text{fall time}}$ was calculated as the time it took for the voltage to reach 0.37 of the fall back to baseline.

Additional measures included the temporal and spatial spread of the events in a recording which included identifying events which were concurrent in time within 5 ms of each other across channels and calculating their spatial spread based on the electrode layout. Peri-stimulus time histograms (PSTHs) involved binning activity in time around specific events, such as the application of pro-convulsant medications, cold saline, auditory stimulation, or electrical stimulation. The bins were one at 100 ms or at other time ranges depending on the treatment. PSTHs and inter-event interval counts were normalized relative to baseline by dividing each bin by the average bins during the baseline recordings before averaging PSTHs across participants.

Event-triggered spectral analyses were performed by taking the 30 seconds around each event (whether the Type 1, 2, or 3 events) of the data sampled at 1000 Hz and then calculating power by taking the real value of the Morlet wavelet coefficient (power) at a 1-Hz spectral resolution using a moving window of 0.5 sec moving every 10 ms, calculated using the Fieldtrip toolbox (www.ru.nl/fcdonders/fieldtrip) (Oostenveld et al., 2011). We then normalized the power at each frequency band by dividing each time step in power per frequency band by the mean power across all windows of time per frequency band. Finally, we averaged the power per the following frequency bands: 0-4, 4-8, 8-15, 15-30, 30-55, and 65-200 Hz.

Cross-covariance measures were calculated by converting the timing of the Type 1, Type 2, and Type 3 events in into 1 ms bins throughout the recording (at a sample rate of 1000 Hz) and then performing a cross-covariance between the event types.

Statistical analysis

All statistical comparisons were performed using non-parametric measures so we did not test for normality. We tested comparisons with the Kruskal–Wallis test for non-equivalence of multiple medians followed by the use of the *post hoc* Tukey-Kramer method to determine statistically separable groups. For all comparisons, we performed calculations by first calculating the mean values per type of neural activity on the per-participant level and then comparing the medians between conditions. Measurements of activity were separated into baseline, during pharmacological manipulation, stimulation (auditory or electrical), or physiological manipulation. This resulted in measurements being taken from distinct samples for the manipulations aside from baseline activity, a period of time which was measured and compared multiply when needed to identify changes in activity. We used the Wilcoxon rank sum test (two-sided) for comparisons between individual medians. We tested if values were significantly different from zero using the Wilcoxon signed rank test. We corrected by adjusting the target p-value (0.05) with a Bonferroni correction for the number of comparisons being done.

Data and code availability. Open source acquisition software, OpenEphys (http://www.open-ephys.org/) and open source waveform sorting software Kilosort (https://github.com/cortex-lab/KiloSort) was used to record and analyze the neural data. Custom Matlab code (version R2019a) in combination with open source code from the Fieldtrip toolbox (http://www.fieldtriptoolbox.org/) was used for the majority of the analyses and is available upon request. The data that support the findings of this study are available from the corresponding author upon reasonable request.